












## RESEARCH ARTICLE

10.1029/2024MS004389

# The Influence of Vertical Resolution on Internal Tide Energetics and Subsequent Effects on Underwater Acoustic Propagation

## Key Points:

- Model vertical resolution impacts internal tide-induced kinetic energy, available potential energy, dissipation, and vertical shear
- Increasing the number of isopycnal layers, up to 48, increases the available potential energy contained in high (third to eighth) vertical modes
- At least 48 isopycnal layers are necessary to minimize variability in sound speed and acoustic propagation caused by the number of layers

L. Hiron<sup>1</sup> , M. C. Schönau<sup>2</sup> , K. J. Raja<sup>1</sup> , E. P. Chassignet<sup>1</sup> , M. C. Buijsman<sup>3</sup> ,  
B. K. Arbic<sup>4</sup> , A. Bozec<sup>1</sup> , E. F. Coelho<sup>5</sup> , and M. S. Solano<sup>6</sup> 

<sup>1</sup>Center for Ocean-Atmospheric Prediction Studies, Florida State University, Tallahassee, FL, USA, <sup>2</sup>Scripps Institution of Oceanography, University of California, San Diego, La Jolla, CA, USA, <sup>3</sup>School of Ocean Science and Engineering, The University of Southern Mississippi, Stennis Space Center, MS, USA, <sup>4</sup>Department of Earth and Environmental Sciences, University of Michigan, Ann Arbor, MI, USA, <sup>5</sup>Applied Ocean Sciences (AOS), LLC, New Orleans, LA, USA, <sup>6</sup>SOFAR Ocean Technologies, San Francisco, CA, USA

## Correspondence to:

L. Hiron,  
[lhiron@fsu.edu](mailto:lhiron@fsu.edu)

## Citation:

Hiron, L., Schönau, M. C., Raja, K. J., Chassignet, E. P., Buijsman, M. C., Arbic, B. K., et al. (2025). The influence of vertical resolution on internal tide energetics and subsequent effects on underwater acoustic propagation. *Journal of Advances in Modeling Earth Systems*, 17, e2024MS004389. <https://doi.org/10.1029/2024MS004389>

Received 17 APR 2024

Accepted 4 JAN 2025

**Abstract** Internal tide generation and breaking play a primary role in the vertical transport and mixing of heat and other properties in the ocean interior, thereby influencing climate regulation. Additionally, internal tides increase sound speed variability in the ocean, consequently impacting underwater acoustic propagation. With advancements in large-scale ocean modeling capabilities, it is essential to assess the impact of higher model resolutions (horizontal and vertical) in representing internal tides. This study investigates the influence of vertical resolution on internal tide energetics and its subsequent effects on underwater acoustic propagation in the HYbrid Coordinate Ocean Model (HYCOM). An idealized configuration with a ridge, forced only by semidiurnal tides and having 1-km horizontal grid-spacing, is used to test two different vertical-grid discretizations, defined based on the zero-crossings of horizontal velocity eigenfunctions and the merging of consecutive layers, with seven distinct numbers of isopycnal layers, ranging from 8 to 128. Analyses reveal that increasing the number of layers up to 48 increases barotropic-to-baroclinic tidal conversion, available potential energy, and vertical kinetic energy, converging with higher layer counts. Vertical shear exhibits a similar pattern but converges at 96 layers. Increasing the number of isopycnal layers, up to 48, increases the available potential energy contained in high (third-to-eighth) tidal baroclinic modes. Finally, sound speed variability and acoustic parameters differ for simulations with less than 48 layers. Therefore, the study concludes that a minimum vertical resolution (48 layers in this case) is required in isopycnal models to accurately represent internal tide properties and associated underwater acoustic propagation.

**Plain Language Summary** Internal tides are waves that undulate along interfaces between waters of different densities inside the ocean and form when tides interact with sloping topography. Like waves at the beach, internal tides can break and mix cold, deep water with warmer surface water, helping to spread heat throughout the water column. This mixing can reduce the amount of heat at the ocean surface, affecting ocean-atmosphere interactions and influencing the climate. Additionally, internal tides can impact acoustic propagation in the ocean interior. In the past decade, realistic numerical simulations have been able to model internal tides. However, model resolution (horizontal and vertical) may impact internal tide properties. This study uses “simplified” simulations with different vertical layers and forced only by tides to investigate the impact of the number of layers on the properties of modeled internal tides and subsequent effects on acoustic propagation. We find that increasing the number of layers up to 48 layers increases the vertical velocity and vertical shear, which have the potential to increase mixing of water and impact the way sound propagates in the ocean interior. Therefore, we conclude that at least 48 layers are required to accurately represent internal tides and associated underwater acoustic propagation.

© 2025 The Author(s). Journal of Advances in Modeling Earth Systems published by Wiley Periodicals LLC on behalf of American Geophysical Union. This is an open access article under the terms of the [Creative Commons Attribution License](https://creativecommons.org/licenses/by/4.0/), which permits use, distribution and reproduction in any medium, provided the original work is properly cited.

## 1. Introduction

Internal tide generation and breaking play a primary role in the vertical transport and mixing in the ocean interior (Ferrari & Wunsch, 2009; Munk & Wunsch, 1998; Vic et al., 2019). The vertical isopycnal displacement induced by internal tides can be as large as ~200 m, with the highest displacements usually observed in the thermocline (Klymak et al., 2011; Park et al., 2008; Rainville et al., 2013). The breaking of internal tides drives significant diapycnal mixing and vertical heat and salt fluxes, resulting in substantial impacts on the heat content of the upper

ocean, affecting ocean-atmosphere interactions, and thereby influencing the climate (Hebert, 1994; Melet et al., 2022). This high-frequency variability induced by internal tides holds significant importance for mixing parameterizations in global climate models (de Lavergne et al., 2020; Olbers et al., 2019). Turbulence mixing in the ocean interior by internal tides participates directly in the maintenance of the Meridional Overturning Circulation (MacKinnon et al., 2017; Stewart et al., 2012). Another significant outcome is the vertical movement of nutrients, essential for primary production and carbon uptake, which in turn has further implications for climate dynamics (Kossack et al., 2023; Tuerena et al., 2019). Moreover, internal tides increase sound speed variability in the ocean, with subsequent effects on underwater acoustic propagation (e.g., Colosi et al., 2013; Noufal et al., 2022; Turgut et al., 2013; Yang et al., 2010). Changes in underwater acoustic propagation have direct applications for sonar performance precision, bioacoustic source localization, acoustic tomography, and underwater acoustic communication (e.g., Erbe et al., 2022; Preisig, 2007).

Internal (baroclinic) tides are internal waves (IWs) generated by the interaction of barotropic tides with topography features in the stratified ocean environment (St. Laurent & Garrett, 2002; Wunsch, 1975). These waves can radiate very far (>1,000 km) from their region of origin (Alford & Zhao, 2007; Buijsman et al., 2016, 2020; Dushaw et al., 1995; Rainville & Pinkel, 2006; Ray & Mitchum, 1996, 1997), and more than 50% of the total baroclinic tidal energy can dissipate locally through wave breaking, wave-wave interactions, and scattering toward higher harmonics and wavenumbers (Eden et al., 2020; Lamb, 2004; Solano et al., 2023; St. Laurent & Garrett, 2002; Vic et al., 2019). Internal tides can also interact with mesoscale eddies, causing these waves to shift from stationary to non-stationary (e.g., Buijsman et al., 2017; Nelson et al., 2019; Ponte & Klein, 2015; Ray & Zaron, 2011; Shriver et al., 2014; Yadidya et al., 2024; Zaron, 2017; Zaron & Egbert, 2014). A recent study found that eddy-internal tide interaction can lead to an enhanced dissipation of internal tides (Wang & Legg, 2023).

Recent computational advancements have allowed the inclusion of tides in high-resolution global ocean models (Arbic, 2022; Arbic et al., 2012, 2018). However, the variation in model parameters and grid spacing can affect how internal tides are represented in these models and their consequent wave-wave and wave-mean flow interactions. For example, the increase in bathymetry resolution generates stronger internal tides at a local scale (Xu et al., 2022). Furthermore, Buijsman et al. (2020) showed that decreasing the horizontal grid spacing from 8 to 4 km in realistic, global HYbrid Coordinate Ocean Model (HYCOM) simulations increased the semidiurnal barotropic-to-baroclinic tidal conversion by 50%. This enhancement in tidal conversion is associated with an increase in the number of vertical modes resolved (from 1 to 2 to 1–5  $M_2$  modes), which also leads to a better representation of wave-wave interactions (Buijsman et al., 2020).

Stewart et al. (2017) reviewed the importance of vertical resolution in resolving the vertical structure of meso- and large-scale horizontal baroclinic flows. They found that increasing the vertical resolution in an Ocean Global Circulation Model can increase sea surface height variance and barotropic and baroclinic eddy kinetic energy due to a better representation of baroclinic modal structures. In the context of internal waves, Nelson et al. (2020) found that decreasing the horizontal grid spacing in regional Massachusetts Institute of Technology general circulation model (MITgcm) simulations from 2 to 0.25 km greatly improves the internal wave frequency spectra and that increasing *only* the number of vertical levels by a factor of three (from 90 to 270 depth levels) does not yield any significant improvement. The latter occurs because, in this case, the horizontal resolution limits the number of modes resolved, as shown in Buijsman et al. (2020). However, increasing both vertical and horizontal grid spacing yielded the best comparison of internal wave frequency spectra to observations (Nelson et al., 2020). Also using regional MITgcm simulations, Thakur et al. (2022) found that increasing the number of vertical levels from 109 to 264 levels for a horizontal grid spacing of  $1/48^\circ$  ( $\sim 2$  km in their domain) improved the representation of small-vertical-scale density and velocity fluctuations, improving the internal wave (IW) field, which, in turn, better represented IW-induced mixing and dispensed the need for the background value of the diapycnal mixing coefficient in the K-Profile Parameterization (KPP). The KPP scheme, proposed by Large et al. (1994), is widely used to represent vertical turbulent mixing in oceanic numerical simulations and has been extensively implemented in various ocean models, including HYCOM.

While the effects of varying vertical grid spacing on internal tides in MITgcm have been investigated, a comprehensive study on the impact of varying the number of vertical levels in HYCOM, which uses isopycnal coordinates in the stratified ocean interior as opposed to constant depth coordinates (or  $z$ -levels) as in MITgcm, is still lacking. Thanks to the isopycnal coordinate system, HYCOM needs significantly fewer vertical layers compared to  $z$ -level models to resolve the same number of vertical modes (Buijsman et al., 2020; Xu et al., 2023).

With the continuous surge in computational power, it has become imperative to understand the implications of increasing resolutions and the benefits they bring to simulations in an attempt to find the optimal equilibrium between computational efficiency and model performance.

There has been an increase in the number of submesoscale-resolving regional and basin-scale HYCOM simulations developed in the past years, such as the  $1/100^\circ$  ( $\sim 1$  km) horizontal grid-spacing simulation for the Gulf of Mexico and  $1/50^\circ$  ( $\sim 2$  km) simulation for the North Atlantic (Chassignet & Xu, 2017; Chassignet et al., 2023; Hiron et al., 2021, 2022; Uchida et al., 2022; Xu et al., 2022, 2023). Recent discussions among oceanographers and ocean modelers center on performing a global HYCOM simulation with tidal forcing and finer horizontal grid-spacing on the order of  $1/50^\circ$ , and even potentially  $1/100^\circ$  in the future, to replace the current state-of-the-art global HYCOM with  $1/25^\circ$  grid spacing. However, the optimal number of layers for such a simulation is still an open question, with a debate surrounding the number of layers needed to resolve a given number of baroclinic modes. Xu et al. (2023) show that, in theory, an HYCOM simulation with sufficient horizontal resolution only requires two layers (i.e., one-layer interface) to resolve the first baroclinic Rossby radius of deformation, as long as the interface is placed at the depth of the zero-crossing of the first baroclinic mode of the horizontal velocity eigenfunction. Similarly, only two-layer interfaces are needed to resolve the second baroclinic Rossby radius of deformation, and so on. Thus, according to Xu et al. (2023), only  $n$  number(s) of layer interfaces are needed to resolve the  $n$ th baroclinic mode of meso- and large-scale motions. However, they also suggest that three-layer interfaces ( $3*n$ ) are required for the maximum amount of energy (kinetic and available potential energy) permitted by a given horizontal grid spacing to be projected onto the first baroclinic mode, assuming that neither horizontal nor vertical grid-spacing are limiting. In other words, one layer interface will “allow” energy to be projected onto the first baroclinic mode, but three layer interfaces are needed to maximize the energy in this mode and not undermine the theoretical capabilities of a given horizontal grid. In this study, we evaluate the optimal number of layers that maximize the energy projected onto the baroclinic modes in the context of internal tides.

This paper investigates the impact of increasing the number of vertical layers in a HYCOM simulation with a 1-km horizontal grid-spacing on (a) the representation of internal tide energetics (kinetic energy and available potential energy) and squared vertical shear, (b) the number of tidal baroclinic modes resolved and the amount of kinetic energy and available potential energy contained in the lower and higher modes, and (c) the subsequent effects on sound speed variability and underwater acoustic propagation. The above will be investigated using an idealized configuration of HYCOM with a  $1/100^\circ$  ( $\sim 1$  km) horizontal grid-spacing, forced solely with semi-diurnal barotropic tide and having a density profile characteristic of the tropics. Different numbers of vertical layers (all isopycnal) and two different types of grid discretization will be employed. The idealized configuration allows us to isolate the internal wave problem and avoid “contamination” from meso- and large-scale motions, wind-driven near-inertial waves, and wave-mean flow interactions. One important characteristic that we are not investigating in this study is the internal wave continuum frequency and vertical wavenumber spectrum, which is also impacted by vertical resolution (e.g., Nelson et al., 2020; Thakur et al., 2022).

## 2. Methodology

### 2.1. Hybrid Coordinate Ocean Model (HYCOM)

The HYbrid Coordinate Ocean Model (HYCOM) is a hydrostatic ocean general circulation model system (Bleck, 2002). Recent modeling advancements, such as smaller grid-spacing and hourly outputs, have allowed the inclusion of both barotropic and internal tidal components into HYCOM and have expanded our understanding of tidal dynamics on a global scale (Arbic, 2022; Arbic et al., 2012, 2018). HYCOM uses isopycnal coordinates in the stratified ocean interior, pressure coordinates near the surface and in the mixed layer, and terrain-following coordinates on the shelves (Chassignet et al., 2003, 2009). HYCOM's unique vertical coordinate system distinguishes it from other global models that use  $z$ -level coordinates, such as MITgcm or the European model NEMO (Madec et al., 2019). In our idealized simulations, only isopycnal coordinates were used.

### 2.2. Idealized Configuration

An idealized configuration is chosen to study the effects of vertical resolution on internal tide energetics without potential contamination from meso- and large-scale motions. The idealized configuration consists of a two-dimensional box with  $1/100^\circ$  horizontal grid spacing, 8,000 grid points in the longitudinal direction, and 4,000 m depth. The simulations use HYCOM version 2.3.01, have hourly outputs, and are only forced by the

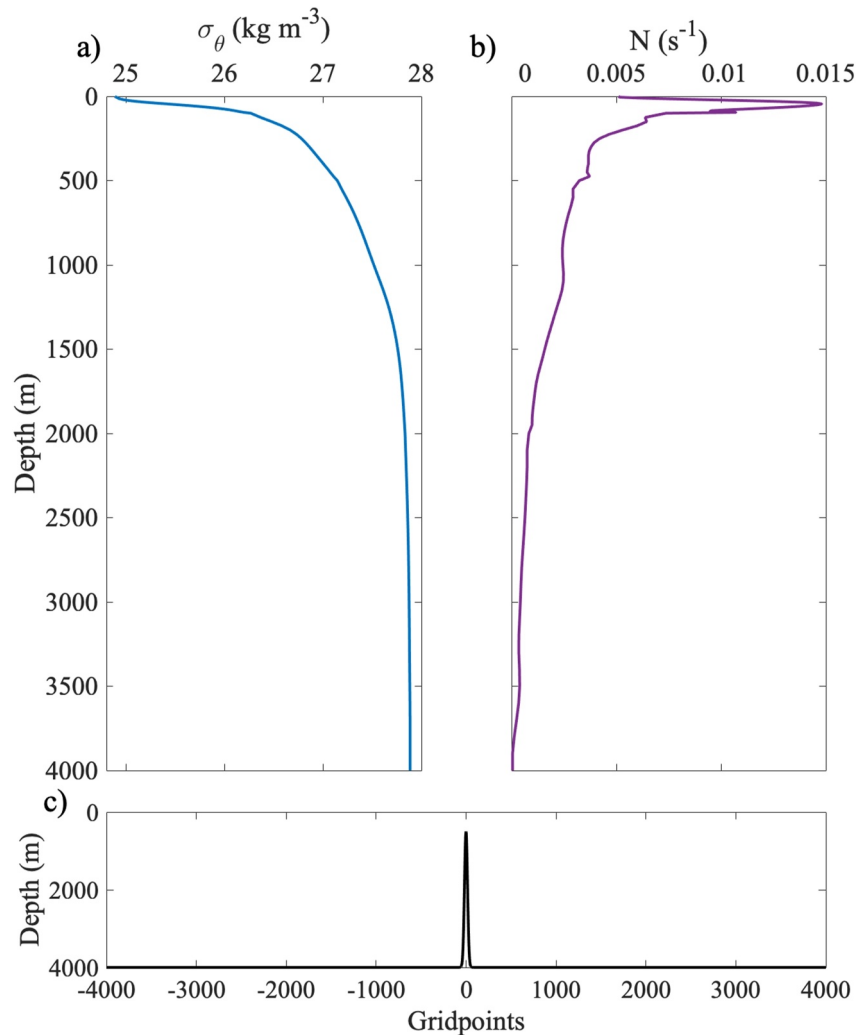


**Figure 1.** (a) Density profile used as the initial condition for all simulations and associated (b) buoyancy frequency. (c) Topography of the idealized configuration, with a 3,500 m high ridge in the middle of the domain.

semidiurnal ( $M_2$ ) tidal constituent.  $M_2$  is the largest lunar constituent, and its internal tide field contains about 70% of all tidal energy (Egbert & Ray, 2003). The amplitude of the barotropic tide used here is equal to the tidal amplitude of the Amazon shelf, an area known for its relatively large tides. The simulations are initialized with a generic density profile representative of the tropics. To avoid freshwater influence from the Amazon shelf region, the “generic” density profile from the tropics is obtained by averaging World Ocean Atlas 2018 climatology (Garcia et al., 2019) over  $17^\circ\text{--}23^\circ\text{N}$  and  $27^\circ\text{--}12^\circ\text{W}$  during the summer months (Figures 1a and 1b), referenced to the surface (sigma zero;  $\sigma_0$ ). This density profile is used for the initial and boundary conditions. The choice of this density profile for the simulations is based on the fact that a generic density profile from the tropics has larger vertical density gradients compared to mid-latitude and polar density profiles. Therefore, in the context of global models, more layers are expected to be needed to correctly resolve the vertical gradients of density profile from the tropics compared to higher latitudes. A ridge with a Gaussian shape was added in the center of the domain with a height of 3,500 m and a standard deviation (also called Gaussian root mean square width) of 17 km (Figure 1c). A Gaussian ridge is preferred over a continental shelf in the idealized configuration for generating internal tides, mainly due to numerical reasons. This choice prevents the generation of “reflecting” waves that can occur when the barotropic tide interacts with the continental shelf in numerical simulations, and allow us to better isolate the impact of the vertical resolution on the internal tides.

Some non-dimensional parameters are provided below to characterize the regime of the baroclinic tides, following Garrett and Kunze (2007) and Buijsman et al. (2010). These parameters are computed based on the following variables of our configuration: the amplitude of the tidal barotropic velocity  $U_0$  over the ridge is  $\sim 0.05 \text{ m s}^{-1}$ , the maximum ridge height  $H$  is 3,500 m, the maximum buoyancy frequency  $N_{\text{max}}$  is  $0.015 \text{ s}^{-1}$ , and the topographic length scale (Gaussian standard deviation;  $\sigma$  or  $L$ ) is 17 km. The criticality of the slope  $\gamma$  is expressed as  $\gamma = \max\left(\frac{1}{\alpha} \frac{dh}{dx}\right)$ , where  $h(x)$  is the topographic height, and  $\alpha = \sqrt{\frac{\omega^2 - f^2}{N^2 - \omega^2}}$ , with  $\omega$  being the  $M_2$  tidal frequency,  $f$  the Coriolis frequency (near zero for our case), and  $N$  the buoyancy frequency. The slope parameter  $\gamma$  for our configuration is  $\sim 2.3$ , that is, supercritical ( $\gamma > 1$ ), which means the ridge slope is steep enough to permit wave-wave nonlinear interactions and well-defined internal wave beams (Balmforth et al., 2002; Buijsman et al., 2010; Garrett & Kunze, 2007). Strong velocity shear along the beams is also present with this regime. The tidal excursion number [ $Ex = U_0/(L\omega)$ ] associated with our configuration is small,  $\sim 0.02$  ( $Ex \ll 1$ ), which guarantees the generation of coherent internal wave beams, with a baroclinic velocity that is substantially larger than barotropic tidal velocity (Jalali et al., 2014). The topographic Froude number [ $Fr_t = U_0/(N_{\text{max}}H)$ ] is also small,  $\sim 1 \times 10^{-4}$  ( $Fr_t \ll 1$ ), which means that the flow is affected by the topography. Thus, with  $\gamma > 1$ ,  $Ex \ll 1$ , and  $Fr_t \ll 1$ , our configuration falls in regime 5 of Garrett and Kunze (2007). This regime allows for the generation of IWs at higher harmonics.

To document the effect of the vertical resolution on internal tides, multiple simulations are carried out keeping all other parameters constant and only varying the numbers of isopycnal layers and grid discretization. Two sets of vertical grid discretizations are tested to examine the dependency of our results on the way the layers are distributed (hereinafter referred to as the *first set* and the *second set of experiments*). In the *first set of experiments*, the interface depths are defined using the zero-crossings of the horizontal velocity eigenfunctions (also called  $u$ -eigenfunctions; Kelly, 2016; Kelly & Lermusiaux, 2016) based on the density profile (Figure 1a). For a simulation of  $n$  layers, the interface depths are defined as the depths of the zero-crossings of the  $(n - 1)$ th mode  $u$ -eigenfunction for the ocean interior, plus the “surface”, considered as the interface at pressure equals zero, and the bottom, providing then a vertical grid with  $n$  number of layers. The rationale for using  $u$ -eigenfunctions to define the layers in an isopycnal model is based on the resolution of baroclinic mode numbers. To resolve a specific mode number in an isopycnal model, the interface layers should coincide with the zero-crossings of the  $u$ -eigenfunction, ensuring that the maximum horizontal velocity occurs within each layer (Stewart et al., 2017; Xu et al., 2023). Defining the vertical grid based on the eigenmodes means that the model is optimal in effective vertical resolution: a simulation with  $n$  layers resolves  $n - 1$  modes (assuming the horizontal grid spacing is not limiting), unlike other grid discretization choices that need many more layers to resolve the same number of modes (Early et al., 2020, 2021). Although we are not solving more than the first few baroclinic modes in these simulations due to limitations in horizontal and vertical resolution (Buijsman et al., 2020), this technique is an objective way to define the interface depths of our simulations. Seven simulations are performed with the following number of vertical layers: 8, 16, 32, 48, 64, 96, and 128 (Figure 2). See Section 2.3 for more information on the vertical mode decomposition.

For the *second set of experiments*, we start with the 128-layer simulation described above and merge consecutive layers to obtain vertical grids with the following number of layers: 8, 16, 32, and 64 layers (Figure 3). Thus, in the second set of experiments, the layer interfaces do not coincide with the depths of the  $n - 1$  mode zero-crossings (except for the 128-layer simulation, which is the same in both sets of experiments). The merging of consecutive layers is a method that has been applied previously in HYCOM with realistic configuration to investigate the impact of the vertical resolution on the large-scale circulation in the North Atlantic (Xu et al., 2023). We adopt the same approach here for the idealized simulations in the context of internal tides. Our objective in testing two different grid discretizations is to assess how the choice of interface depth locations affects the results. Later, we will demonstrate that variations in tidal energetics and vertical shear are more influenced by the number of layers than by the grid discretization itself.

Zonal boundaries feature a relaxation time ranging from 0.1 to 1 day, accompanied by high viscosity, to avoid reflection on these boundaries. All vertical physics, including the KPP scheme, are turned off. Note that the publicly available version of HYCOM does not support strictly 2-dimensional simulations—at least five grid points are needed on the zonal and meridional directions to compute second-order derivatives. To address this, we introduced five additional grid points in the meridional direction and enforced a zero meridional velocity ( $v$ ) at each time step. This approach allows us to maintain a computationally efficient simulation while preventing wave

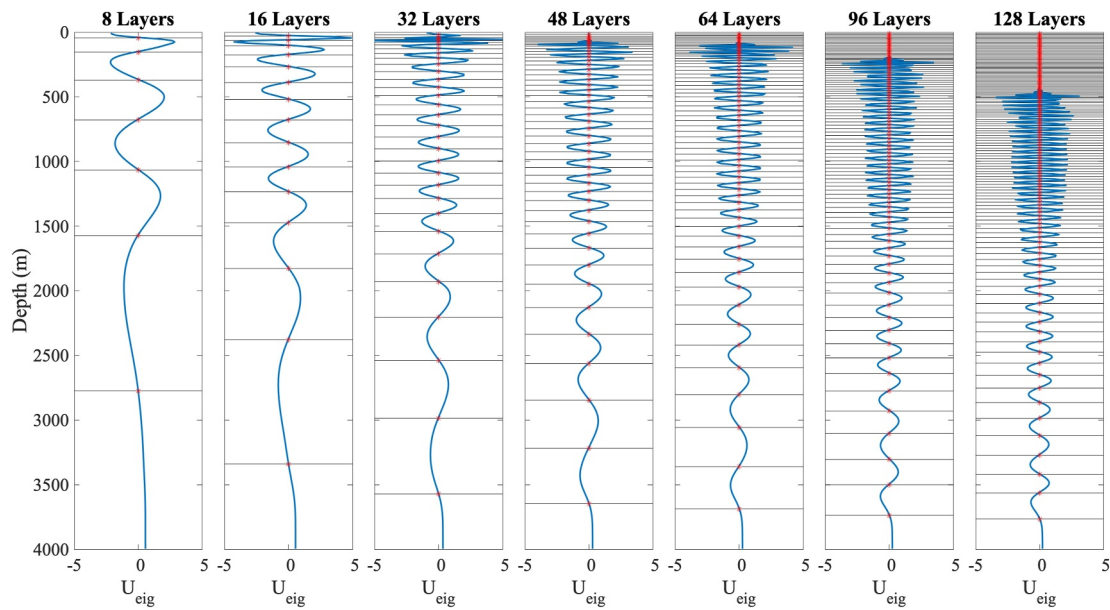


**Figure 2.** Distribution of the interface depths (black horizontal lines) for the first set of experiments based on the depths of the zero-crossings (black lines) of the horizontal velocity eigenfunctions (blue curves). These grids are used to initialize the first set of simulations with 8, 16, 32, 48, 64, 96, and 128 layers.

reflections in the meridional direction. The configuration is symmetric with respect to the ridge; thus, for practicality, the energy diagnostics are done on one side of the domain and integrated from the ridge to a point 250 km from the ridge. The simulations are run for 30 days with hourly outputs (a total of 721 time steps). All analyses, except for the KE spectra, are conducted over four tidal periods after the model reaches equilibrium, which occurs after 8 days. The KE spectra are computed over the remaining days after equilibrium, a total of 22 days.

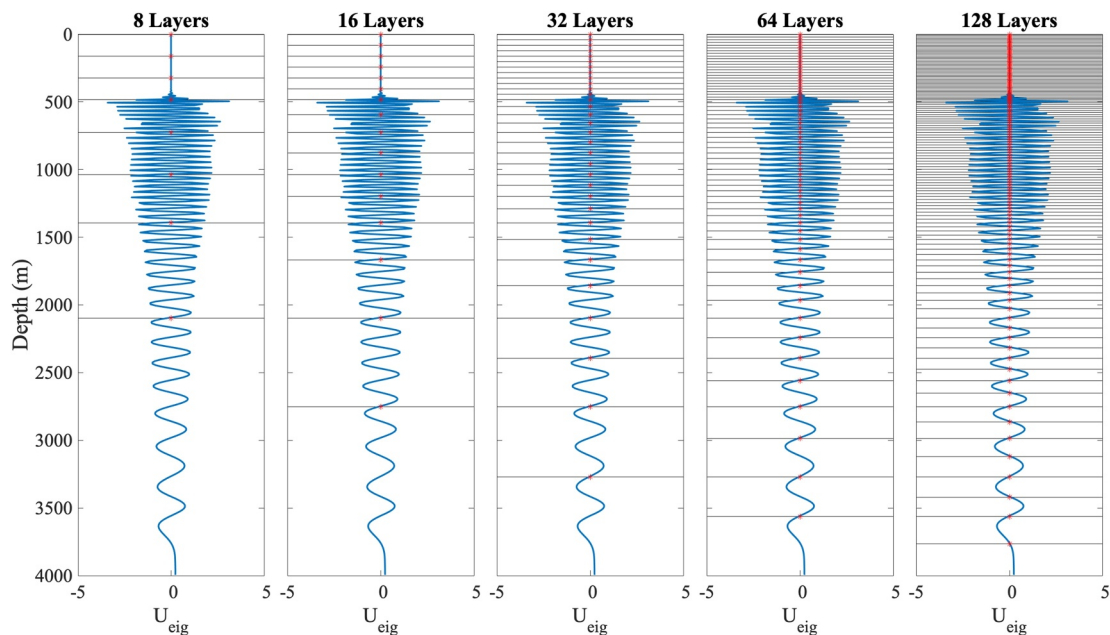


**Figure 3.** Distribution of interface depths (black horizontal lines) for the second set of experiments based on merging consecutive layers starting from the 128-layer simulation defined by the zero-crossings of the  $u$ -eigenfunction (blue curves in all subplots) with 8, 16, 32, 64, and 128 layers. Note that the 128-layer simulation is the same in both sets.

### 2.3. Vertical Mode Decomposition

Baroclinic fields can be decomposed into vertical standing waves (normal modes) that propagate horizontally (Gerkema & Zimmerman, 2008). The vertical velocity ( $w$ -) eigenfunction  $\mathcal{W}_n(z)$  of the mode  $n$  can be found by solving the following Sturm-Liouville equation

$$\frac{\partial^2 \mathcal{W}_n(z)}{\partial z^2} + \frac{N^2}{c_n^2} \mathcal{W}_n(z) = 0 \quad (1)$$

where  $c_n$  is the eigenspeed,  $N = \sqrt{-\frac{g}{\rho_0} \frac{\partial \rho(z)}{\partial z}}$  is the buoyancy frequency computed using the initial density profile  $\rho$  (Figure 1a),  $g$  is the acceleration of gravity,  $\rho_0$  is the constant density associated with the Boussinesq approximation, taken here as  $1,027 \text{ kg m}^{-3}$ , and  $z$  is the vertical coordinate. The eigenfunctions obey the orthogonality condition  $\frac{1}{H} \int_0^H \mathcal{W}_n \mathcal{W}_m dz = \delta_{mn}$ , where  $m$  and  $n$  are different modes, and  $\delta_{mn}$  is the Kronecker delta function. The boundary conditions are a rigid lid at the surface and bottom ( $\mathcal{W}_n = 0$  at  $z = 0, H$ ). The eigenspeed is expressed as

$$c_n = \frac{\sqrt{\omega^2 + f^2}}{k_n} \quad (2)$$

where  $\omega$  and  $f$  are the  $M_2$  and Coriolis frequencies, respectively, and  $k_n$  is the horizontal wavenumber. The horizontal velocity eigenfunction (or  $u$ -eigenfunction) is then found by taking the derivative of  $\mathcal{W}_n(z)$ ,

$$\mathcal{U}_n(z) = \frac{\partial \mathcal{W}_n}{\partial z}(z), \quad (3)$$

and normalizing it by the depth-averaged  $\mathcal{U}_n$  amplitude, that is,  $\sqrt{\frac{1}{H} \int_0^H \mathcal{U}_n^2(z) dz}$ , where  $H$  is the water column depth, following the same method as previous studies (Buijsman et al., 2014, 2020; Early et al., 2021; Gerkema & Zimmerman, 2008; Gill, 1982; Kelly, 2016; Kelly et al., 2012; Raja et al., 2022, 2024). The  $w$ -eigenfunction  $\mathcal{W}_n$  is normalized by the depth-averaged  $\mathcal{W}_n$  weighted by  $N^2$ , that is,  $\sqrt{\frac{1}{H} \int_0^H \mathcal{W}_n^2(z) N^2(z) dz}$ , as in Kelly and Lermusiaux (2016). Thus, after normalization,  $\mathcal{U}_n$  is unitless and  $\mathcal{W}_n$  has units of  $s$ . The  $u$ -eigenfunction for mode numbers 8, 16, 32, 48, 64, 96, and 128 (blue lines) and the corresponding zero-crossings (horizontal black lines) are shown in Figure 2.

### 2.4. $M_2$ Energetics and Vertical Shear

All quantities described below were computed in the original HYCOM grid (isopycnal layers), including tidal energetics, squared vertical shear, barotropic-to-baroclinic conversion, and dissipation. The only quantities computed on interpolated fields are the  $u$ - and  $w$ -eigenfunctions and, thus, the modal kinetic energy and available potential energy (Section 2.4.4). The  $u$ - and  $w$ -eigenfunctions were estimated by interpolating the density profile in the original vertical grid into an equidistant vertical grid, with a one-m vertical grid spacing, using a Piecewise Cubic Hermite Interpolating Polynomial.

#### 2.4.1. Tidal Barotropic-To-Baroclinic Energy Conversion and Dissipation

Tidal barotropic-to-baroclinic energy conversion is computed as in Kelly et al. (2012):

$$C(x, t) = -p'_{\text{bottom}}(x, t) u_{\text{btp}}(x, t) \frac{\partial H(x)}{\partial x} \quad (4)$$

where  $u_{\text{btp}}$  is the barotropic tidal velocity,  $p'_{\text{bottom}}$  is the perturbation pressure at the bottom, and  $H$  is the depth of the water column. The barotropic velocity is obtained by depth-averaging the velocity field, and the perturbation pressure is computed by removing the time-mean and the depth-mean pressure from the pressure field. The

vertically-integrated baroclinic energy flux  $F_p$  can be computed as the product of the baroclinic velocity perturbation  $u'_{bcl}$  and the perturbation pressure  $p'$  integrated vertically in the water column:

$$F_p(x, t) = \int_0^z u'_{bcl}(x, z, t) p'(x, z, t) dz. \quad (5)$$

The baroclinic velocity is obtained by subtracting the barotropic velocity from the total velocity field. To compute the baroclinic velocity perturbation, the pointwise and time-average baroclinic velocity is subtracted from the baroclinic velocity field. The residual between the tidal barotropic-to-baroclinic energy conversion and the baroclinic energy flux divergence integrated over a domain provides an indirect estimation of the amount of energy dissipated  $D$  locally/within the domain:

$$D = C - \nabla \cdot F_p \quad (6)$$

#### 2.4.2. Kinetic Energy and Available Potential Energy

The available potential energy (APE) is computed following Gill (1982) and Kundu (1990):

$$\text{APE} = \frac{1}{2} \rho_0 N^2 \zeta^2 \quad (7)$$

where  $N$  is the buoyancy frequency at time zero, and  $\zeta$  is the displacement of the isopycnals relative to their position at time zero. Kang and Fringer (2010) remarked that the equation above (APE<sub>3</sub> in their paper), derived from linear theory, is used in internal wave calculations for slowly varying density fields and that another equation (APE<sub>2</sub> in their paper) is more suitable to account for strong nonlinear and nonhydrostatic effects. In this paper, the results using the two equations were almost identical, in agreement with the fact that HYCOM is a hydrostatic model and that our density profile does not present any vertical density gradients that are too sharp (the domain has a horizontally uniform stratification). Thus, we choose to use the APE equation presented above following Gill (1982) and Kundu (1990).

The total baroclinic kinetic energy KE is computed as follows:

$$\text{KE}_{bcl} = \frac{1}{2} (u_{bcl}^2 + w^2) \quad (8)$$

where  $u_{bcl}$  is the baroclinic zonal velocity, and  $w$  is the vertical velocity computed using the continuity equation. The vertical KE is computed using only the vertical velocity  $w$ .

#### 2.4.3. Squared Vertical Shear

Squared vertical shear  $S^2$  is computed using both the baroclinic zonal and vertical velocity components, as follows

$$S^2 = \left( \frac{\partial u_{bcl}}{\partial z} \right)^2 + \left( \frac{\partial w}{\partial z} \right)^2. \quad (9)$$

Conversion, baroclinic KE, APE, and vertical shear were computed after the model reached a stable state, after 200 hr.

#### 2.4.4. Modal Energetics

Following Gerkema and Zimmerman (2008), Kelly et al. (2012), and Buijsman et al. (2014, 2020), and using Equations 1 and 3, we can find how much KE and APE is contained in each vertical mode. For that, first, we compute the modal amplitudes of the zonal velocity  $\hat{u}_n$  by projecting the  $u$ -eigenfunctions onto the vertical profiles of horizontal velocity as done in Raja et al. (2022, 2024):



$$\hat{u}_n = \frac{1}{H} \int_0^H \mathcal{U}_n(z) u(z) dz. \quad (10)$$

$\hat{u}_n$  has units of  $\text{m s}^{-1}$ . We then compute the horizontal velocity associated with each mode by multiplying the modal amplitudes by the  $u$ -eigenfunctions:

$$u_n(z) = \hat{u}_n \mathcal{U}_n(z). \quad (11)$$

The modal amplitude of the vertical velocity associated with mode  $n$  is obtained as follows:

$$\hat{w}_n = \frac{1}{H} \int_0^H \mathcal{W}_n(z) w(z) N^2(z) dz, \quad (12)$$

$$w_n(z) = \hat{w}_n \mathcal{W}_n(z). \quad (13)$$

The modal isopycnal vertical displacement  $\zeta_n$  is:

$$\hat{\zeta}_n = \frac{1}{H} \int_0^H \mathcal{W}_n(z) \zeta(z) N^2(z) dz, \quad (14)$$

$$\zeta_n(z) = \hat{\zeta}_n \mathcal{W}_n(z). \quad (15)$$

Since  $\mathcal{W}_n$  after normalization has units of s,  $\hat{w}_n$  has units of  $\text{m s}^{-2}$  while  $\hat{\zeta}_n$  has units of  $\text{m s}^{-1}$ . Therefore,  $w_n$  has units of  $\text{m s}^{-1}$  while  $\zeta_n$  has units of m. Modal KE and APE are then computed following Equations 7 and 8. Depth-integrated modal KE and APE can also be computed directly from the modal amplitudes as done in Kelly et al. (2012) and Buijsman et al. (2014) and the results are the same as multiplying the modal amplitudes by the eigenfunctions and then integrated vertically as done here.

## 2.5. Sound Speed and Underwater Acoustic Propagation

### 2.5.1. Sound Speed

The sound speed  $c_s$  ( $\text{m s}^{-1}$ ) was computed following Mackenzie (1981)'s equation:

$$c_s = 1448.96 + 4.591 T - 5.304 \times 10^{-2} T^2 + 2.374 \times 10^{-4} T^3 + (S - 35)(1.340 - 1.025 \times 10^{-2} T) + 1.630 \times 10^{-2} Z + 1.675 \times 10^{-7} Z^2 - 7.139 \times 10^{-13} T Z^3.$$

where  $T$  is the in situ temperature in  $^{\circ}\text{C}$ , converted from the HYCOM potential temperature,  $S$  is salinity, and  $Z$  is depth (positive values). Temperature and salinity were first interpolated to 1 m depth surfaces, using a Piecewise Cubic Hermite Interpolating Polynomial, prior to calculating sound speed.

### 2.5.2. Underwater Acoustic Propagation

Using the model sound speed, Bellhop 3D was used to model acoustic propagation. Bellhop 3D is available from the Ocean Acoustics Laboratory Acoustic Toolbox (<http://oalib.hlsresearch.com/AcousticsToolbox>; Porter, 2011). Bellhop is a ray-tracing model that can trace propagation pathways using either 3D or 2D pressure fields. Bellhop 3D was run for a 1,500 Hz source placed at 20 m depth at the ridge using each of the 18 HYCOM model hourly time steps. The model was run in semi-coherent mode to increase sensitivity to ray phases and output acoustic transmission loss (TL), a measure of acoustic loss from both attenuation and spreading (Urick, 1982). The idealized HYCOM model output for each time step, which is strictly zonal, was replicated in the meridional direction so that some 3D acoustic impacts may be seen. The goal was to examine the sensitivity of the upper-ocean sound speed structure and acoustic propagation to the internal tide layers at relatively short ranges (<150 km). Additionally, we calculated the sonic layer depth (SLD), defined as the depth of subsurface sound speed maximum above which an acoustic duct can form, the below-layer gradient (BLG), defined as the

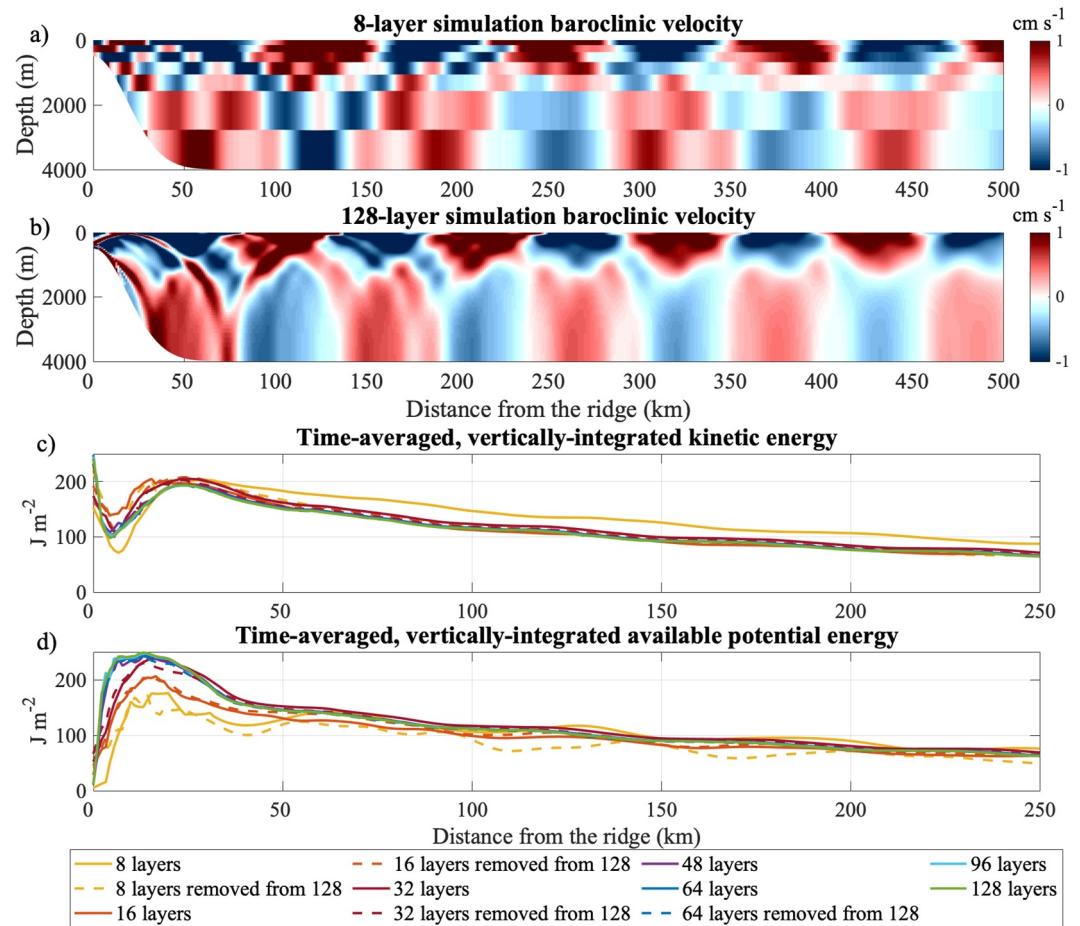


**Figure 4.** Snapshot of tidal baroclinic velocity for the (a) 8-layer and (b) 128-layer simulations forced solely by semidiurnal frequency, and with a  $1/100^\circ$  ( $\sim 1$  km) horizontal grid spacing. Time-averaged, vertically-integrated (c) kinetic energy and (d) available potential energy. Solid lines are the simulations with layers defined using the zero-crossings of  $u$ -eigenfunctions (first set of experiments), and the dashed lines are the simulations with layers defined by merging layers from the 128-layer simulation (second set of experiments). Note that the  $x$ -axis range in (c) and (d) focuses on the first 250 km from the center of the ridge.

gradient in sound speed in the 100 m transitional layer below the SLD, and the in-layer gradient (ILG), defined as the gradient of sound speed in the sonic layer. An acoustic surface-layer duct is a layer where sound is refracted upward from the SLD and reflected downward from the surface, allowing it to travel long distances without dissipation. Together, the SLD, ILG, and BLG can be indicators for surface-layer duct propagation (Colosi & Rudnick, 2020; Helber et al., 2012; Urlick, 1982).

### 3. Tidal Energetics and Squared Vertical Shear

#### 3.1. Baroclinic Kinetic Energy and Available Potential Energy Spatial Patterns

A snapshot of the baroclinic velocity field for the 8- and 128-layer simulations, with grid-spacing defined based on the  $u$ -eigenfunctions (first set of experiments), is shown in Figures 4a and 4b. The wave beams are clearly seen radiating from the ridge in both simulations, in agreement with the properties of our configuration with a supercritical ridge and low excursion length (see Section 2.2) and previous studies (Buijsman et al., 2010; Garrett & Kunze, 2007; Jalali et al., 2014). The 128-layer simulation has wave beams with more details and smaller structures when compared to the 8-layer simulation, which has much coarser vertical grid spacing; however, the ability of the 8-layer simulation to resolve the wave beams is still noteworthy. The presence of wave beams is due to the superposition of baroclinic modes (Gerkema & Zimmerman, 2008).

It is notable that the peaks in baroclinic velocity, or internal wave beam bounces, both at the surface and at the bottom, are not at the same place for the 8- and 128-layer simulations for the same time-snapshot; there is a lag in space. Further in the manuscript, we show that this lag is due to differences, among simulations, in the theoretical (and simulated) wavelength and phase speed for the first baroclinic mode. Values of wavelength and phase speed for the first baroclinic modes decrease with the increase in the number of layers up to 48 layers and remain constant for further increases in the number of layers beyond 48.

The spatial pattern of the time-averaged, depth-integrated baroclinic KE and APE across the domain is shown in Figures 4c and 4d. Due to the symmetry of the domain, only one half is shown, and we provide a zoomed view within the first 250 km away from the center of the ridge. The time-averaged, vertically-integrated baroclinic KE shows the same spatial pattern across simulations with different vertical resolutions: a peak at  $\sim 24$  km away from the ridge, and a smooth decay further from it (Figure 4c). Roughly the same values of KE are found for all simulations independent of the grid-discretization and number of layers, except for the two simulations with 8 layers and, to some extent, the 16-layer simulations, at locations between 12 and  $\sim 60$  km away from the ridge. In contrast, APE magnitude differs more among simulations with different numbers of layers up to 48 layers, especially within the first 50 km from the ridge, and maintains a similar magnitude in the simulations with higher layer counts (Figure 4d). With the addition of more layers beyond 48 layers, the results converge, independent of the grid discretization, highlighting the importance of adding isopycnal layers over modifying the grid discretization. Additionally, the difference between different types of grid discretizations (i.e., the two sets of experiments) is smaller among simulations with the same number of layers than the difference between simulations with different numbers of layers. One maximum peak in APE is present at  $\sim 15$  km with a value of  $250 \text{ J m}^{-3}$  for simulations with at least 48 layers. For the two 16-layer simulations, the peak of maximum APE is  $200 \text{ J m}^{-3}$ , whereas the peak is as low as  $160 \text{ J m}^{-3}$  in the 8 layers of the first set of experiments.

The baroclinic KE and APE peaks are not too far from the point of maximum steepness of the ridge ( $\sim 20$  km) and, consequently, the location of maximum tidal barotropic-to-baroclinic energy conversion. It is important to note that KE and APE are of the same order of magnitude and that both decay away from the ridge. The decay in tidal energy away from the source has been previously documented and attributed, among others, to wave-wave interactions and subsequent decay to smaller scales, which are then affected by numerical and viscous dissipation (e.g., Eden et al., 2020; Lamb, 2004; Solano et al., 2023; St. Laurent & Garrett, 2002; Vic et al., 2019).

### 3.2. Domain-Integrated Tidal Energy Conversion, Baroclinic Kinetic Energy, and Available Potential Energy

Tidal barotropic-to-baroclinic energy conversion, APE, baroclinic KE, and vertical KE, integrated from the center of the ridge ( $x = 0$ ) to 250 km from the ridge, for the two different vertical grid-discretization and different numbers of layers are shown in Figure 5. Tidal energy conversion differs slightly between simulations, with a small increase in averaged conversion with the increase in the number of layers for both sets of simulations up to 32 layers, and it remains constant with a further increase in layers (Figure 5a). Domain-integrated baroclinic kinetic energy decreases with the increase in the number of layers, independently of the grid discretization (Figure 5b). The values go from  $3.6 \times 10^{10} \text{ J}$  for the 8-layer simulation of the first set of experiments to  $2.5 \times 10^{10} \text{ J}$  for the 128-layer simulation. Note that the value of KE for the 8-layer simulation of the first set of experiments stands out from the other simulations. We will see later that, for this simulation, less energy is being dissipated. The domain-integrated barotropic kinetic energy (not shown) is very similar among simulations, with a slight decrease with the increase in the number of layers, from  $1.0 \times 10^{10} \text{ J}$  for the 8-layer simulations to  $0.9 \times 10^{10} \text{ J}$  for the 128-layer simulation.

The domain-integrated APE increases with an increase in vertical layers until 48 layers, maintaining consistency in the simulations with higher layer counts ( $3.2 \times 10^{10} \text{ J}$ ) independently of the grid discretization (Figure 5c). This result agrees with the findings from Figure 5b and highlights the importance of increasing the number of layers over adjusting the grid discretization. Consistent with Figure 4, domain-integrated APE is of the same order of magnitude as domain-integrated baroclinic kinetic energy. Last, the domain-integrated vertical KE appears to increase with the increase in the number of layers in simulations having up to 32 layers, then slightly decrease until reaching constant vertical KE among simulations for those with at least 48 layers. While the vertical kinetic energy ( $\frac{1}{2} w^2$ ) is considerably smaller by two orders of magnitude than the horizontal baroclinic kinetic energy, changes in vertical kinetic energy are directly related to changes in the vertical displacement of isopycnals, which

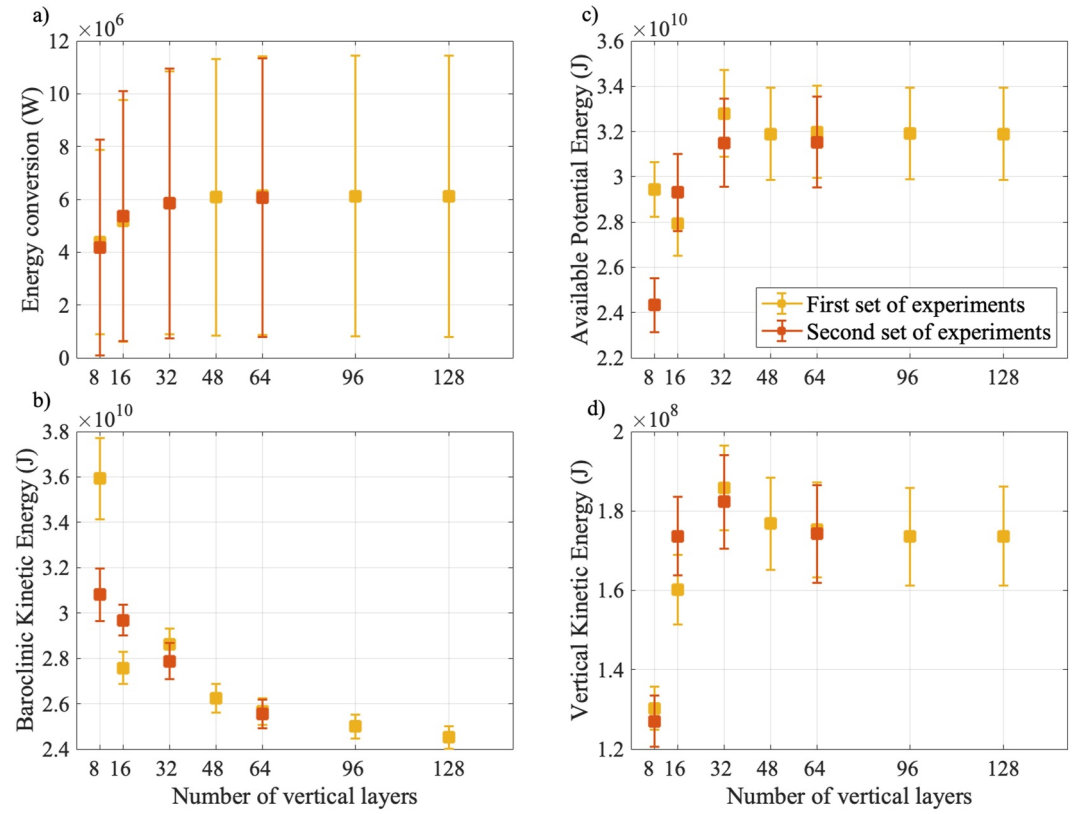


**Figure 5.** (a) Domain-integrated tidal barotropic-to-baroclinic energy conversion ( $W$ ), (b) baroclinic (horizontal + vertical) kinetic energy ( $J$ ), (c) available potential energy ( $J$ ), and (d) vertical kinetic energy ( $J$ ) as a function of the number of vertical layers for two grid-discretizations: layers defined using the zero-crossings of  $u$ -eigenfunctions (yellow; the first set of experiments), and layers defined by merging layers from the 128-layer simulation (orange; the second set of experiments). All the above were integrated spatially from 0 to 250 km from the center of the ridge, and the error bars are the temporal standard deviation over four tidal cycles.

can impact underwater acoustic propagation (Section 5) and the mixing of water properties. This underscores the significance of vertical kinetic energy, prompting us to illustrate how this characteristic evolves with alterations in the number of layers.

Dissipation exhibits a similar pattern to the barotropic-to-baroclinic tidal convergence (Table 1 and Figure 5a); dissipation increases with the increase in the number of layers until 32 layers, then slightly decreases for simulations with more than 48 layers, and remains constant after 96 layers. The overall increase in dissipation with the increase in the number of layers could be due to an increase in wave-wave interactions for simulations with higher layer counts, resulting in the development of more small-scale features and increased horizontal shear, ultimately leading to greater dissipation. Notice the low value of dissipation for the 8-layer simulation of the first set of experiments compared to the dissipation of other simulations—this is in agreement with the higher values of baroclinic kinetic energy for this simulation (Figures 4 and 5b).

At least two model parameters directly affect the dissipation of internal tides: the coefficient of quadratic bottom friction ( $c_b$ —parameter name in HYCOM) and the diffusion velocity for biharmonic thickness diffusion ( $thkdf4$ ). The first, as the name indicates, dissipates energy in the bottom mixed layer through bottom friction, and the second dissipates energy by smoothing isopycnal interfaces. The quadratic bottom drag has been shown to have a small impact on internal tide dissipation (Buijsman et al., 2016). However, to confirm that changes in these parameters do not impact our results, sensitivity experiments were performed varying both parameters. In the simulations presented so far,  $c_b$  and  $thkdf4$  are set as  $2.5 \times 10^{-3}$  and  $0.01 \text{ m s}^{-1}$ , respectively, which are the standard for realistic and idealized HYCOM simulations. To test the influence of those parameters, twin simulations with isopycnal layers defined based on the first set of experiments with 32 and 96 layers were performed with different  $c_b$  and  $thkdf4$ . We first set  $c_b$  as zero while keeping  $thkdf4$  as  $0.01 \text{ m s}^{-1}$ , and then set  $thkdf4$  to zero,

**Table 1**

*Dissipation (MW) Estimated as the Residual Between the Tidal Barotropic-To-Baroclinic Energy Conversion and Baroclinic Energy Flux Divergence Integrated From 0 to 250 km From the Center of the Ridge for the First and Second Sets of Simulations*

Method	Number of layers						
	8	16	32	48	64	96	128
First set of experiments	1.0	2.6	3.4	3.5	3.4	3.3	3.2
Second set of experiments	2.1	2.9	3.5	–	3.4	–	–

*Note.* The vertical grid of the second set of simulations (second line in this table) is defined by merging subsequent layers from the 128-layer simulation defined by the zero-crossings of the  $u$ -eigenfunctions (the first set of experiments). Because of that, there is only one 128-layer simulation. The number of subsequent layers merged is a multiple of two (2, 4, 8, and 16), and gives rise to the second set of experiments with 64, 32, 16, and 8 layers, respectively. No simulations with 48 and 96 layers are present in this method since those numbers are not a multiple of 128.

while keeping  $c_b$  as  $2.5 \times 10^{-1}$ . When the bottom drag was set to zero, we found that the baroclinic kinetic energy and the APE for both 32- and 96-layer simulations increased by less than  $0.01 \times 10^{10}$  J ( $<0.3\%$  of increase) [not shown]. When the biharmonic thickness diffusion was set to zero, the baroclinic KE and APE increased by less than  $0.05 \times 10^{10}$  J ( $<1.5\%$  of increase) for both 32- and 96-layer simulations. The increases in baroclinic KE and APE associated with these two dissipation parameters were substantially smaller than the energy variation due to the number of layers.

### 3.3. Kinetic Energy Frequency Spectra

The kinetic energy frequency spectra of the simulations with different numbers of vertical layers presented similar overall patterns independent of the grid discretization (Figure 6). It is important to note that even the simulations with only 8 layers reproduce all the peaks, which would likely be a challenge for models with only eight  $z$ -levels, as highlighted by Xu et al. (2023). The frequency forcing is semidiurnal. Wave-wave interactions lead to a transfer of energy to peaks at the frequencies multiple of the source frequency; in this case, peaks at  $M_4, M_6, M_8, M_{10},$  and  $M_{12}$  (e.g., Sutherland & Dhaliwal, 2022). A similar amplitude is seen for the  $M_2$  frequency independent of the number of layers. At higher frequencies, nevertheless, more energy is found in simulations with fewer layers. This is in agreement with the larger values of baroclinic KE found in simulations with fewer layers (Figure 5) and with the larger depth-integrated KE for the 8-layer simulation, especially from 50 to 250 km. The reason is because, in the 8-layer

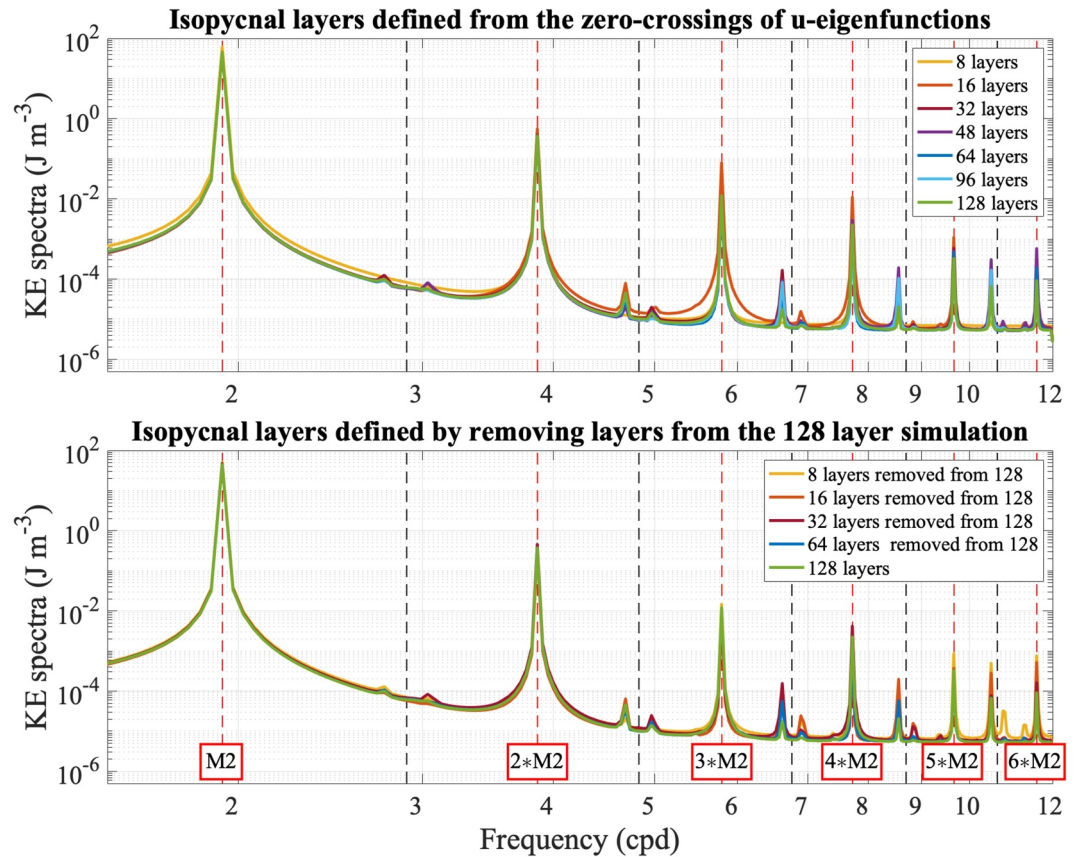


**Figure 6.** Baroclinic kinetic energy frequency spectra at 100 m depth, averaged over 0–250 km from the ridge, for different numbers of layers for the first set of experiments (upper) and the second set of experiments (lower). Note that the 128-layer simulation (green line) is the same in both sub-figures.

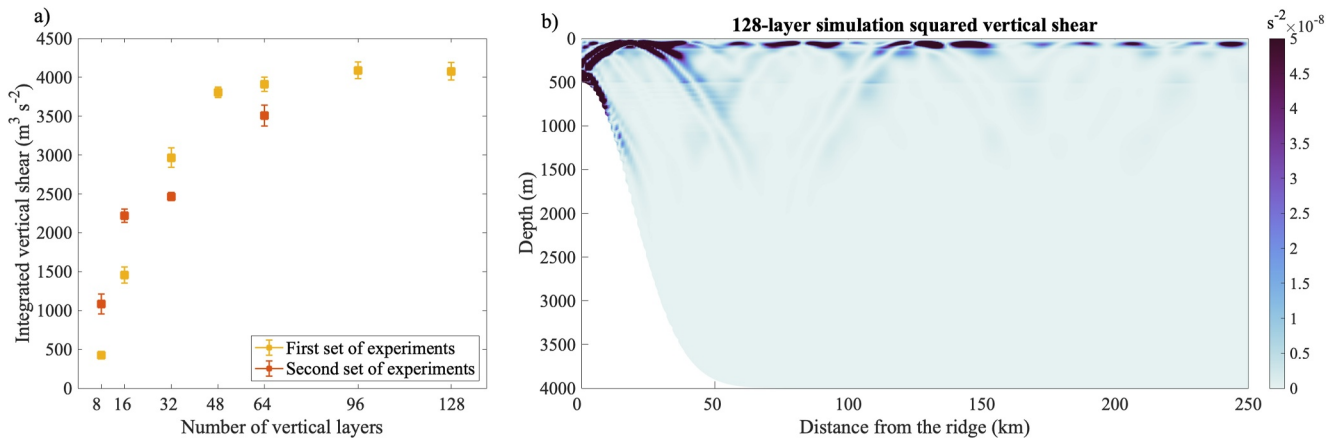


**Figure 7.** (a) Same as Figure 5a, but for the domain-integrated squared vertical shear. (b) Snapshot of the squared vertical shear for the 128-layer simulation.

simulations, more energy is projected onto the lower modes (in particular on the first two baroclinic modes; not shown), and those modes travel for longer distances and dissipate slower than the higher modes. It is important to note that we focus our analyses on 0–250 km because it is where the largest differences between the simulations occur. Beyond 250 km, the simulations start to converge in terms of KE and APE.

Peaks on each side of odd numbers of cycles per day ( $M_3$ ,  $M_5$ , etc.) are associated to the higher order interactions between the subharmonics (excited around  $M_2/2$ ) due to parametric subharmonic instability (PSI), or triad resonant instability (TRI) (Bourget et al., 2013) and the parent wave  $M_2$  or super-harmonics  $M_4$ ,  $M_6$  excited due to resonant triad interactions (Sutherland & Jefferson, 2020; Varma & Mathur, 2017). In the case of inviscid flows (viscosity being zero), PSI excites the subharmonic waves at exactly half the forcing frequency (Koudella & Staquet, 2006). In realistic scenarios, flows are never inviscid, so due to TRI, two peaks are observed around half the forcing frequency, and as viscosity increases (or Reynolds number decreases) the peaks move further away from half the forcing frequency (Bourget et al., 2013; Joubaud et al., 2012). For more information on excitation of both subharmonic and superharmonic in internal waves, as well as triadic resonance, we invite the reader to consult Staquet and Sommeria (2002), Dauxois et al. (2018), and Varma et al. (2023).

### 3.4. Squared Vertical Shear

The domain-integrated squared vertical shear increases with the increase in the number of layers for the two different vertical-grid discretization and levels off from the 96 to 128-layer simulations (Figure 7a). The difference is significant, with values ranging from  $\sim 425 \text{ m}^3 \text{ s}^{-2}$  for the 8-layer simulation to  $\sim 4,100 \text{ m}^3 \text{ s}^{-2}$  for the 96- and 128-layer simulations for the first set of experiments. The 96- and 128-layer simulations presented higher values and more defined patterns of squared vertical shear, in particular where wave beams are located (Figure 7b), contrasting from the lower resolution simulations that presented more diffuse and larger wave beams, leading to lower values of squared vertical shear (not shown). We notice lower shear values in the 32- and 64-layer simulations of the second set of experiments compared to their counterparts in the first set of experiments. This discrepancy is likely related to the fact that the latter has more layers in the upper 200 m, better resolving the high amplitudes of vertical shear in the upper ocean.

High values of vertical shear associated with internal tides can lead to wave breaking and subsequent mixing in the ocean. Many ocean models parameterize mixing using the KPP vertical mixing scheme. A recent study by Thakur et al. (2022) showed that high-resolution models resolving internal tides exhibited higher vertical shear and increased KE variance at the high vertical-wavenumber IW continuum, similar to observations, when the background component of the KPP vertical mixing scheme is turned off. In addition to the impact of the background KPP, the work presented here emphasizes the importance of carefully selecting vertical grid coordinates, as variations in vertical resolution can significantly affect internal-tide-induced vertical shear.

The Richardson number, expressed as the ratio of the squared buoyancy frequency to the squared vertical shear, is an indirect way of measuring mixing due to shear instability. Values smaller than 0.25 indicate the flow is

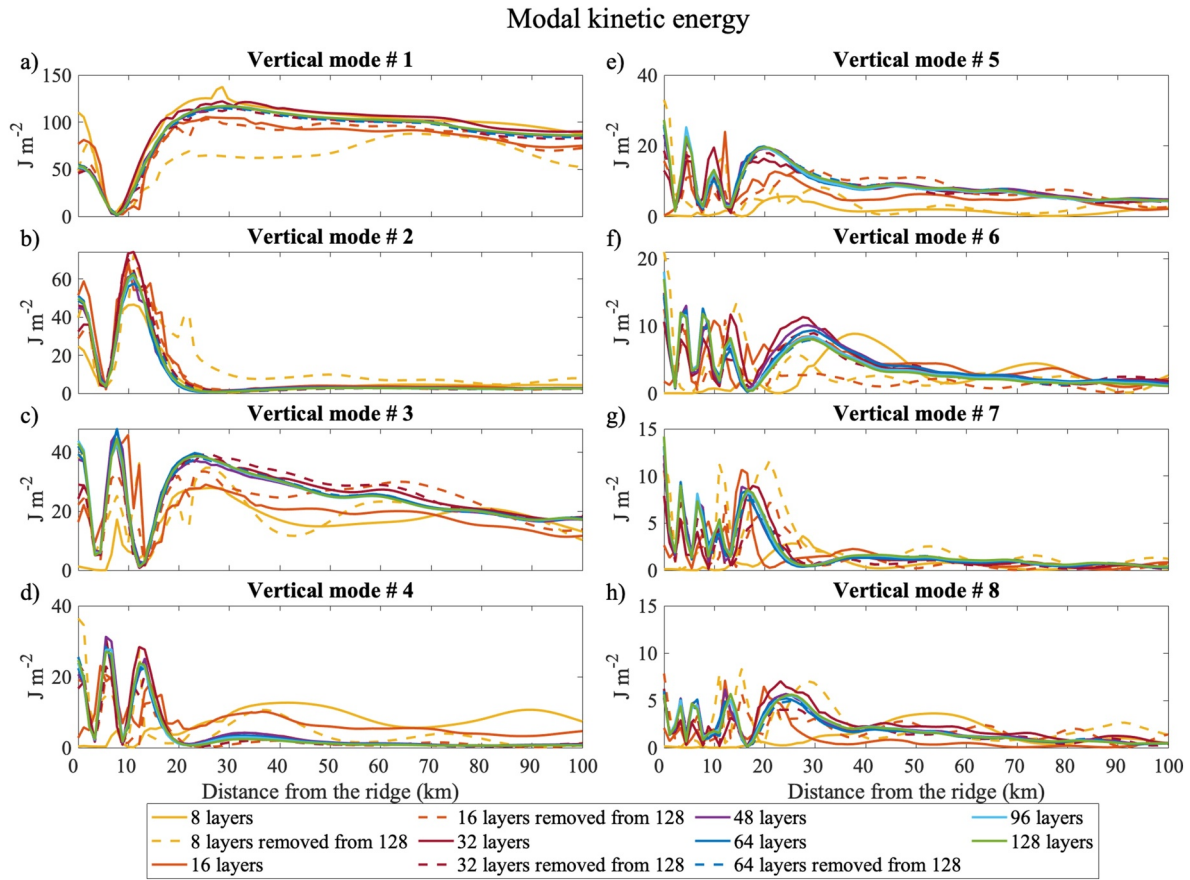


**Figure 8.** Vertically integrated, time-averaged contribution of each baroclinic mode on the total kinetic energy, from the first to the eighth baroclinic mode, for all simulations. Note that the ordinate axis varies for the different modes.

dynamically unstable and prone to turbulent mixing. In our simulations, although there is a reduction in stratification where the internal tide beams are the strongest—in the upper 300 m and within 40 km from the center of the ridge (not shown)—the Richardson number remains much larger than 1 for the prescribed density field, even where the stratification is reduced. However, the Richardson number might be smaller for other stratifications such as mid-latitude density fields.

#### 4. Modal Kinetic Energy and Available Potential Energy

KE and APE for baroclinic modes one to eight are shown in Figures 8 and 9. For all simulations, KE and APE projected only on the first eight vertical modes, even for the 8-layer simulations. When comparing the total KE and APE with the sum of the modal KE and APE for the first 250 km from the ridge, we find that less than 3% of the total KE and APE is not projected onto modes, with the exception of the 8-layer simulation of the second set of experiments, for which 4.5% of the total KE was not projected onto the vertical modes. The residual (total KE and APE minus the sum of modal KE and APE) decreases with the increase in the number of layers.

For the first 100 km from the ridge, more than half (~60%) of the total modal KE is contained in the first baroclinic mode for all the simulations, ~7% is contained in the second baroclinic mode, and 17% in the third baroclinic mode (Figures 8a–8c). From 100 to 250 km from the ridge, around 80% of the total modal KE is contained in the first baroclinic mode for all simulations, ~3% in the second baroclinic mode, and ~11% in the third baroclinic mode. Modal KE converges for simulations with at least 32 layers independent of the grid discretization. For the simulations with 8- and 16-layers, modal KE appears to be lower, on average, than the higher-resolution ones for the third and fifth baroclinic modes and larger for the fourth baroclinic mode. Most energy (>90%) is contained in the first 5 modes. The energy contained in higher modes decays rapidly away from the ridge, in agreement with previous studies (Lamb, 2004; Solano et al., 2023; St. Laurent & Garrett, 2002).

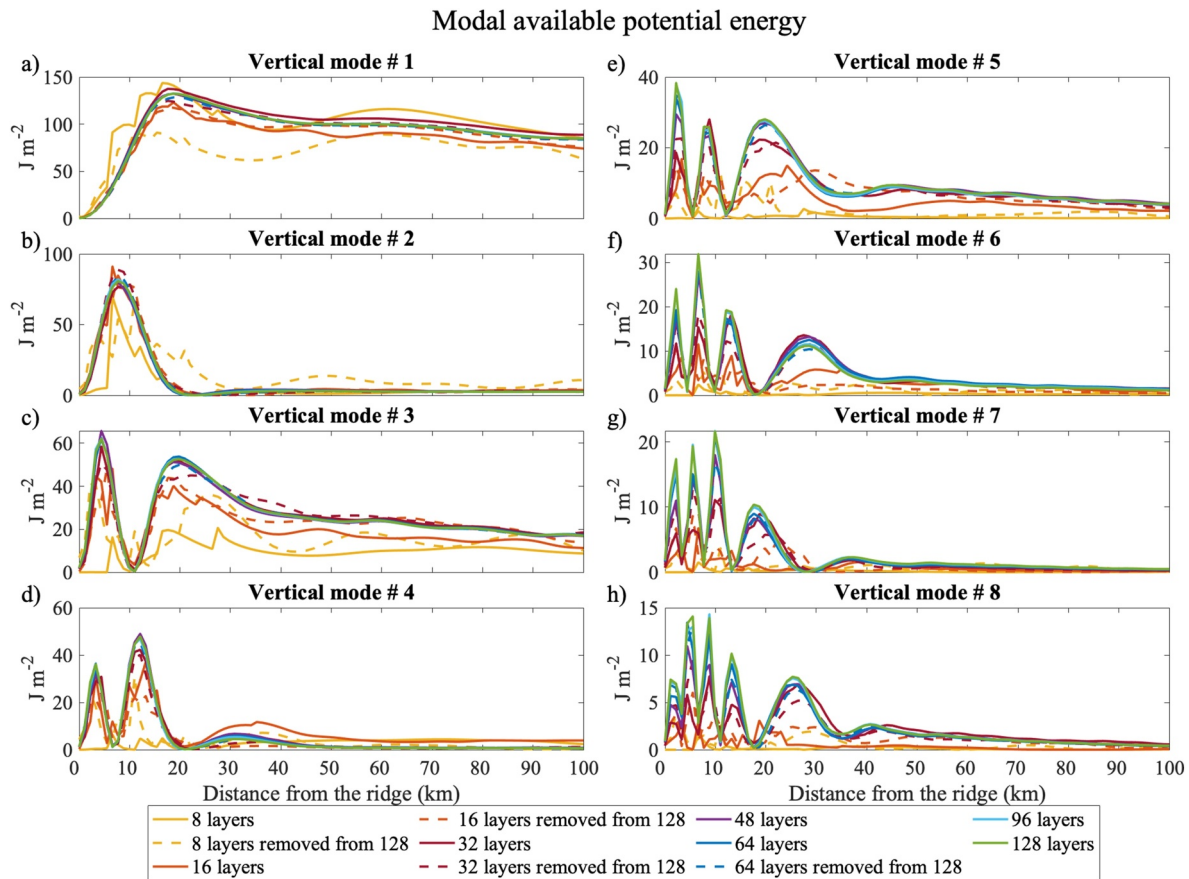


Figure 9. Same as Figure 8, but for modal available potential energy focused on the first 50 km from the center of the ridge.

The differences caused by having different numbers of layers are more evident in the modal available potential energy (Figure 9). There is a clear increase in available potential energy with the increase in the number of layers, in particular for modes equal to or higher than the third baroclinic mode (Figures 9c–9g). Modal APE converged for simulations with at least 48 layers independent of the grid discretization. For the first 100 km from the ridge, and for simulations with at least 48 layers, 60% of the total modal APE is contained in the first baroclinic mode. This number increases with the decrease in the number of layers. On average, for the first 100 km from the ridge, around 7% is contained in the second baroclinic mode, and around 16% is contained in the third baroclinic mode (Figures 9a–9c). From 100 to 250 km from the ridge, around 84% of the total modal APE is contained in the first baroclinic mode for all simulations, ~3% in the second baroclinic mode, and ~10% in the third baroclinic mode (this value is smaller for the 8-layer simulations and the 16-layer one of the first set of experiments). The modal APE in the higher modes decayed rapidly away from the ridge compared to the energy associated with the first and third baroclinic modes. In summary, at least 48 vertical layers were needed to accurately resolve the APE associated with higher modes, in particular from the third up to the eighth baroclinic mode. Both kinetic and available potential energy presented near-zero values for modes higher than mode eight.

For both modal KE and APE, the two different grid discretizations presented large differences, particularly for the 8-layer simulations. More differences between different vertical grids are expected for simulations with less vertical layers because the interface-depths are further apart; thus, their location relative to the zero-crossings of  $u$ -eigenfunctions or  $w$ -eigenfunctions have larger impact on the total horizontal and vertical velocities. The difference in KE and APE between the two grid discretizations decreases with the increase in the number of layers.

Phase speed and wavelength of the baroclinic tides for modes 1–10, estimated using the Sturm-Liouville equation, are shown in Figure 10. Both phase speed and wavelength decreased with the increase in the number of layers until 48 layers and remained constant with additional layers, independent of the grid discretization. Phase speed and wavelength for each mode decreased from ~2.5 m s<sup>-1</sup> and 110 km in the 8-layer simulations to 2.2 m s<sup>-1</sup> and



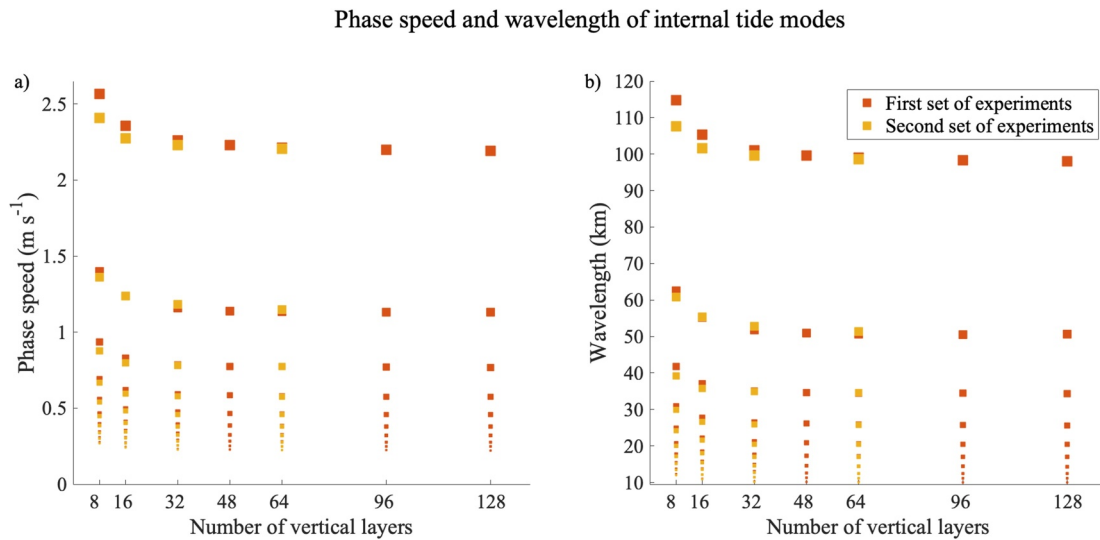


**Figure 10.** Internal tide (a) phase speed and (b) wavelength for the first 10 baroclinic modes (from larger to smaller squares) for both types of grid-discretizations computed from the Sturm-Liouville equation.

100 km in the 48-layer simulation, respectively, for the first baroclinic mode. In fact, the wave beams were observed to be located closer to the ridge in simulations with at least 48 layers, and they extended further from the ridge when decreasing the number of layers (see Figure 4 for 8- and 128-layers), in agreement with Figure 10. The difference between phase speed and wavelength among simulations with different numbers of layers decreases with the increase in mode number.

The distance between subsequent wave beam bounces at the surface and bottom ( $\sim 100$  km; Figure 4) is similar to the wavelength of the first baroclinic mode (Figure 10). This means that internal wave beams bounce up and down over one mode-one wavelength for realistic stratification as well, similar to the case of idealized, in-depth constant stratification in Gerkema and Zimmerman (2008).

It is important to note that, generally, the resolution of baroclinic modes can be limited by horizontal and vertical numerical grid spacings. In numerical modeling, it is considered that a given ocean feature is resolved if there are at least  $2\pi$  grid points along the feature (e.g., Griffies & Treguier, 2013). This is consistent with the concept of *effective resolution*, which refers to the smallest resolved scale in a model that remains largely unaffected by numerical dissipation caused by discretization errors (Skamarock, 2004). In general, the *effective resolution* in ocean models is considered to be about 6 to  $10\Delta x$  (Griffies & Treguier, 2013; Soufflet et al., 2016). A comprehensive discussion on the *effective resolution* in ocean models is provided by Le Sommer et al. (2018).

For our configuration, the wavelengths of the first eight baroclinic modes are equal to or larger than 10 km (Figure 10), meaning that our choice of horizontal grid spacing ( $\sim 1$  km) is small enough to resolve them, considering that roughly six to ten grid-points are needed to solve a given baroclinic mode (Griffies & Treguier, 2013; Soufflet et al., 2016). Thus, we can assume that the resolution of the first eight baroclinic modes is limited only by the vertical resolution. However, beyond the eighth baroclinic mode, the horizontal grid spacing becomes limiting. Previous studies based on mooring observations have shown that the first few modes account for more than 80% of the internal wave kinetic energy (e.g., MacKinnon & Gregg, 2003; Rainville et al., 2010). Therefore, our simulations resolve the most energetic baroclinic modes associated with internal tides.

## 5. Sound Speed Variability and Underwater Acoustics Propagation

For this section, we focus on the first set of experiments.

### 5.1. Sound Speed Variability

Sound speed depends on temperature, salinity, and depth. Thus, the up-and-down vertical displacement of isopycnals driven by internal tides induces sound speed variability. Findings from Section 3 show that simulations

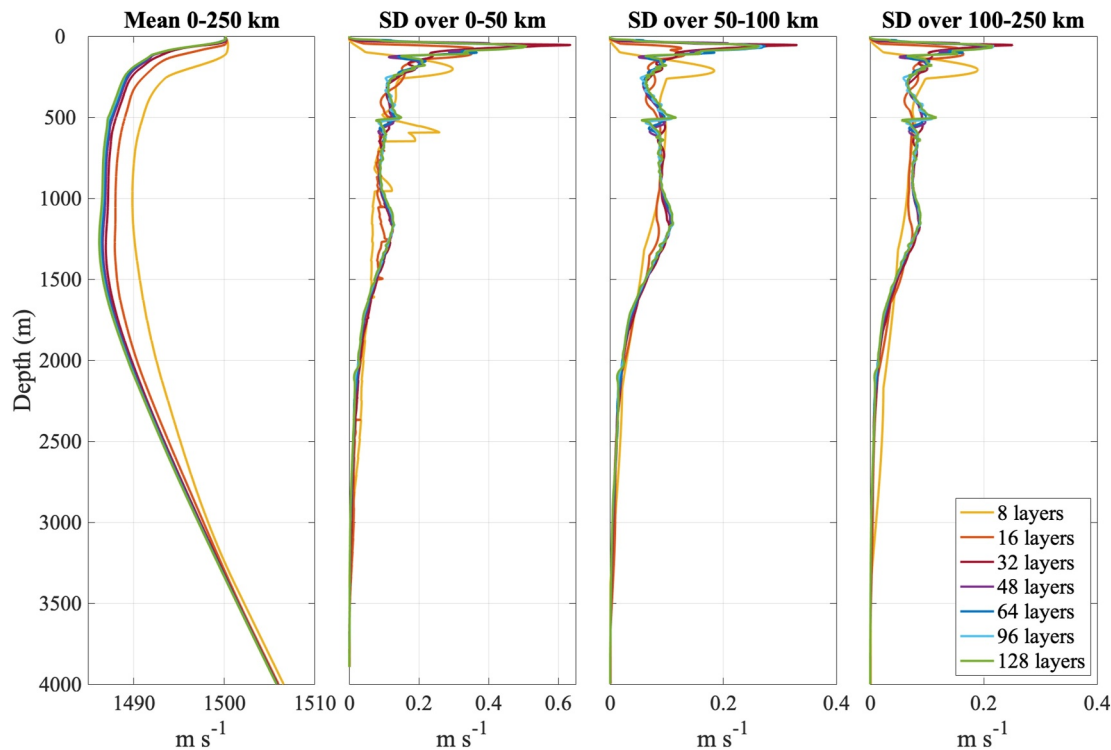


**Figure 11.** Mean sound speed averaged over 0–250 km from the center of the ridge, and sound speed standard deviation (SD) averaged over 0–50 km from the center of the ridge, 50–100 km, and 100–250 km for the simulations with 8, 16, 32, 48, 64, 96, and 128 layers (the first set of experiments) Note that the range of the x-axis differs between the subplots.

with a higher number of layers, up to 48 layers, presented higher vertical kinetic energy and available potential energy (Figures 5c and 5d). Both these quantities are also related to vertical isopycnal displacement. In fact, we find differences among the simulations in the vertical profiles of mean sound speed and an increase in sound speed variability with the increase in the number of layers, from 8 up to 48 layers, with the variability changing very little with additional layers (Figure 11). The 8-layer simulation presented a larger sonic layer and, consequently, deeper SLD and a deep channel (centered around ~1,000 m) that is less pronounced compared to the other simulations with a higher number of layers. With the increase in layer count, the SLD decreases, and the deep channel becomes more pronounced, with equilibrium after 48 layers.

The greatest variability, as measured by the standard deviation over each hourly time step for a total of four tidal periods, was found to be in the upper 250 m for all simulations, although the peak of maximum variability varied, with variability peaks at ~210 m depth for 8 layers and at ~110 m depth for 16 layers. For the higher-layer simulations (>16 layers), the peak sound speed variability was found at shallower depths (~60 m). Although the 32-layer simulation's depth of maximum variability was at ~60 m, the amplitude was  $0.1 \text{ m s}^{-1}$  (25%) larger compared to the simulations with higher layer count for the 0–50 km range from the ridge. The larger amplitude in the 32 layers compared to the other simulations with higher layer count is persistent as we go further from the ridge (50–100 km and 100–250 km), but with a smaller difference in amplitude compared to 0–50 km. A secondary peak in sound speed variability was observed around ~1,150 m with similar magnitudes for simulations with at least 32 layers. This peak is smaller in amplitude than the one in the 16-layer simulation and non-existent in the 8-layer simulation. A similar pattern was found for the second set of experiments (not shown). The depth of the peaks in sound speed variability corresponds to the depths of the peaks in APE variability (not shown), which is to be expected since both variables are affected by the vertical displacement of isopycnals.

## 5.2. Underwater Acoustic Propagation

To briefly revisit the acoustic variables, the SLD refers to the depth where subsurface sound speed reaches a maximum, above which an acoustic duct may form. The BLG describes the sound speed gradient within the 100-

m transitional layer beneath the SLD. The in-layer gradient (ILG) represents the sound speed gradient within the sonic layer itself. The differences among simulations in sound speed average and variability shown in Figure 11 have an effect on the acoustic transmission loss (TL) and underwater acoustic parameters SLD, BLG, and ILG (Figures 12 and 13). The transmission loss (1,500 Hz source at 20 m depth at ridge location) was greatest for the 8-layer simulation and decreased with the increase in the number of layers up to 64 layers, with no significant change for higher layer count (Figure 12). In the 64-, 96-, and 128-layer simulations, we observed a periodic transmission on a semidiurnal timescale (white bands), with two surface layer propagation pathways appearing about every 12 hr. This signal is better explored in the next figure. For 48 layers, shorter periodicity was observed, whereas in the 32 layers, only one weak surface transmission was observed every ~12 hr. For 8 and 16 layers, surface layer propagation was weakest, with TL > 75 dB.

The SLD becomes shallower with the increase in the number of layers up to 64 layers, reaching equilibrium afterward (Figure 12). This result is in agreement with the sound speed averaged profiles from Figure 11a. The depth of the sonic layer varies from over 40 m for the 8 layer model and ~30 m for the 16-layer simulation, to ~20 m for the 32- and 48-layer simulations, and ~15 m for the simulations with at least 64 layers, in agreement with the mean profile of sound speed (Figure 11). For the BLG, simulations with at least 48 layers presented similar values of BLG, and larger gradient values compared to 8-, 16-, and 32-layer simulations. For ILG, the convergence happens at 64 layers, similar to TL and SLD, with higher values for the simulations with at least 64 layers. Although the shallowness of the SLD for the higher-layer simulations means the source is deeper than the SLD, such as around time step 7, when shoaling of the SLD at around 30 m range (Figure 12) caused a noticeable increase in TL. However, in general simulations with a greater number of layers had sound speed gradients more conducive to supporting the acoustic surface duct.

To expand on the acoustic transmission loss seen in Figure 12, we look at a depth-dependent snapshot of the transmission loss for all simulations (Figure 13). We observed a few differences among simulations. First, TL was greater for simulations with lower numbers of layers. As the number of layers increases, TL gradually diminished, reaching its lowest point in the 64-layer simulation. Beyond this point, TL stabilized, indicating a consistent behavior with the addition of extra layers, and in agreement with Figure 12. Second, the rays were more defined, sharper, and with a higher density of rays with the increase in the number of layers, up to 64 layers. The 8-layer simulation, for example, presents fewer propagation pathways, with little transmission in a deeper sound channel. As the number of layers increased, so did the number of propagation pathways. This caused greater propagation that converged in the deeper sound speed channel (centered ~1,000 m depth), and nearer to the surface for higher numbers of layers, up to 64. Propagation in the surface layer is observed in simulations with at least 64 layers. The reflection from the surface and refraction at the SLD are nearly absent in the 8- and 16-layer simulations for distances larger than 40 km from the ridge, and weaker in the 32- and 48-layer simulations. At a higher number of layers, results were similar. The differences between the simulations in surface and sub-surface duct propagation are likely related to the difference in sound speed gradients introduced by the addition of layers.

The convergence zones, where the rays meet at the surface, were less defined and further spaced apart in the 8-layer simulation. This spacing decreases with the increase in the number of layers up to 48 layers, similar to the wavelength of the first baroclinic mode (Figure 10). Simulations with lower numbers of layers, in particular the 8- and 16-layer simulations, have a weaker deep sound channel (Figure 11a), which could be affecting the reflection angle of the sound waves and, consequently, where they converge.

## 6. Discussion and Conclusions

This study investigates the influence of vertical resolution on internal tide energetics and subsequent effects on underwater acoustics propagation in HYCOM. Two grid-discretizations with seven different numbers of layers, ranging from 8 to 128 isopycnal layers, were tested using a 2-D, idealized configuration, only forced with semidiurnal tides, with ~1 km horizontal grid-spacing and a ridge in the center of the domain. In the first set of experiments, the interface depths are defined using the zero-crossings of the  $u$ -eigenfunctions, whereas in the second set of experiments, the interface depths are defined by the merging of consecutive layers starting from the 128-layer simulation of the first set of experiments.

The results show that increasing the number of layers up to 48 layers increased the domain-integrated barotropic-to-baroclinic tidal conversion, available potential energy, and vertical kinetic energy, maintaining the same values in simulations with higher layer counts, independently of the grid-discretization. Domain-integrated vertical shear

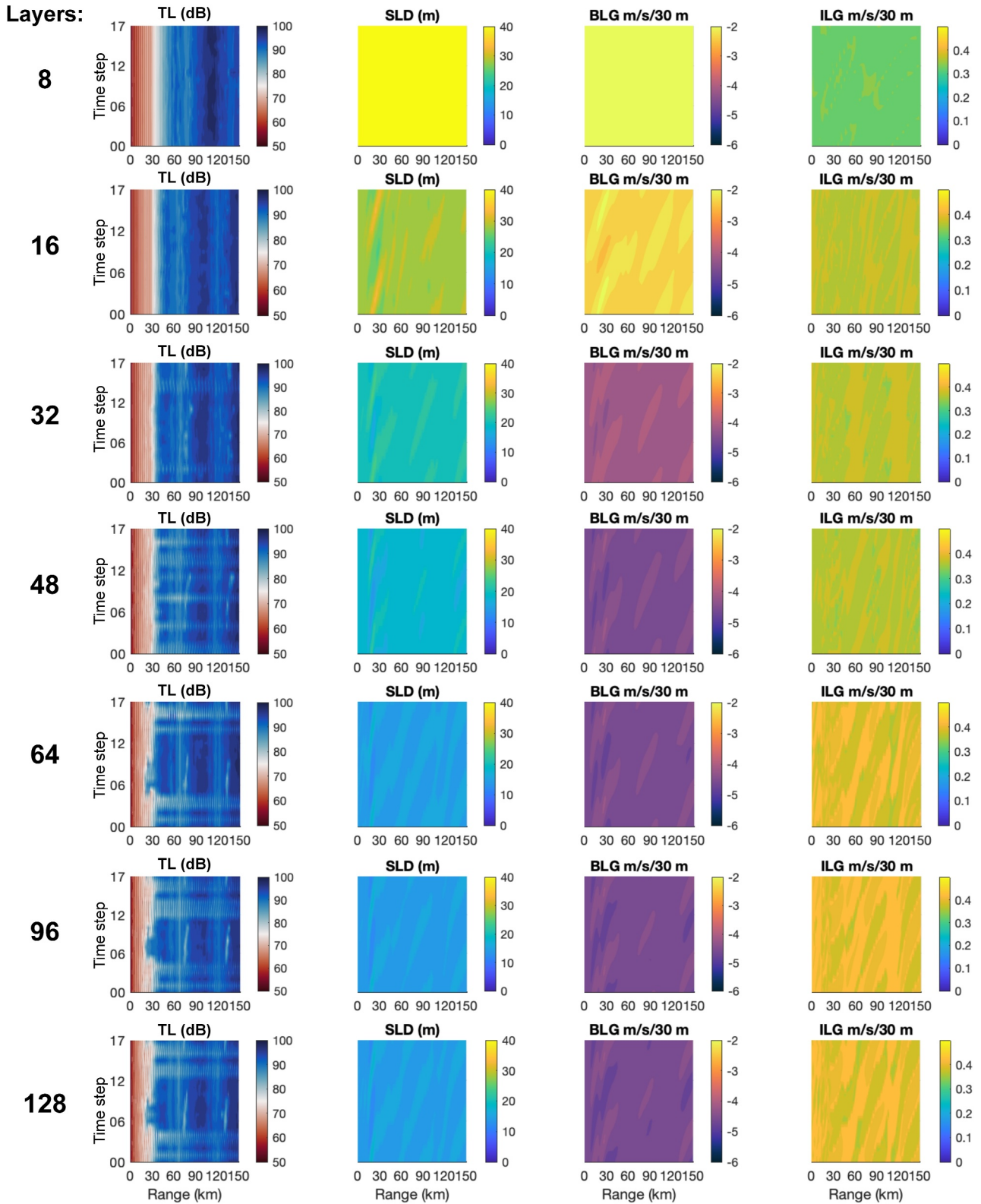


**Figure 12.** Underwater acoustic properties for the first set of experiments (from 8 to 128 layers, each line shows a different simulation). Acoustic transmission loss (TL; first column) in decibels (dB) with a 1,500 Hz source at 20 m depth at ridge location; sonic layer depth (SLD; second column); below-layer gradient (BLG; third column); and in-layer gradient (ILG) defined as the gradient of sound speed in the sonic layer (fourth column). Sub-plots show the time step in the y-axis in hours and the distance from the ridge in kilometers (the zero value is the center of the ridge).

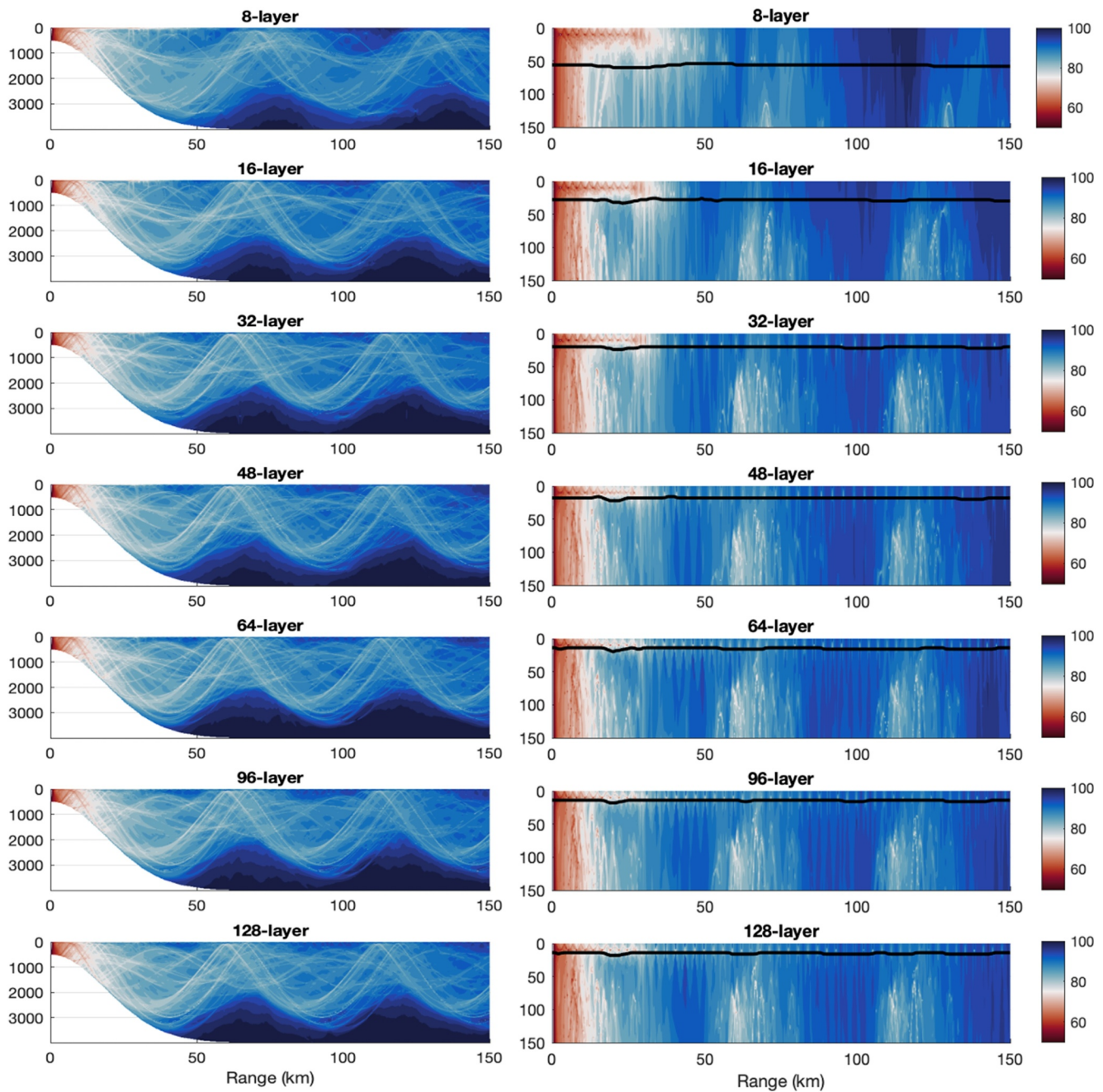


**Figure 13.** Snapshot of acoustic transmission loss (TL; first column) in decibels (dB) with a 1,500 Hz source at 20 m depth at ridge location for the entire water column (left) and focused on the upper 150 m (right) for the first set of experiments (from 8 to 128 layers). The black line is the depth of the sonic layer.

exhibits a similar pattern but reaches a maximum at 96 layers instead of 48, and remains constant with the addition of more layers. Domain-integrated kinetic energy, on the other hand, decreased with the increase in the number of layers. Therefore, as the number of layers increases—up to 48 layers—more energy is directed into the vertical displacement of isopycnals, resulting in higher vertical KE and APE, while less energy is allocated to baroclinic kinetic energy. The study also finds that simulations with at least 48 layers fully resolved the available potential energy contained in the third to eighth tidal baroclinic mode. The wavelength and phase speed for the first 10 baroclinic modes decreased with the increase in the number of layers, up to 48 layers. Thus, increasing the number of layers increased the vertical density and horizontal velocity gradients of the flow, shown in the increase of energy in higher modes and squared vertical shear, both impacting internal tide-induced vertical transport.

Although differences were observed among simulations with a lower number of layers, it is important to note that even the 8-layer simulations were able to reproduce internal tide patterns, such as wave beams and the 12 peaks in the kinetic energy spectrum. In the case of a  $z$ -level model, it would be needed at least three times that to obtain similar results as the isopycnal coordinates, according to Buijsman et al. (2020) and Xu et al. (2023). Additionally, the 8-layer simulations were able to resolve the same number of vertical modes (8 vertical modes) as the other simulations, even if the amount of energy projected onto the higher modes was smaller. This result indicates that simulations with a minimum of  $n$  layers can project energy up to the  $n$ th vertical mode, provided that the horizontal grid spacing is not limiting. However, we find that more layers lead to a higher amount of energy projected on higher modes for both KE and APE, and that the convergence in energy projected on the higher (up to eighth) modes occurs in simulations with the number of layers between 32 and 48. This means that, on average, 4 to 6 layers between the zero-crossings are adequate to fully resolve a given mode. This study also shows that increasing the number of isopycnal layers is more efficient in terms of representing internal tide energetics over grid discretization adjustments.

The increase in the number of layers also impacts sound speed variability and underwater acoustic propagation. Acoustic analyses show an increase in sound speed variability, in particular in the upper 200 m, and subsequent changes in underwater acoustic properties, with the addition of layers until 48 layers for sound speed variability and 64 layers for underwater acoustic propagation, with not much changes observed with additional layers. We find that for simulations with less than 64 layers, the transmission loss was greater, and with less defined and more diffuse sound wave beams. The SLD and ILG both become shallower with the increase in the number of layers up to 64 layers. The same happens for BLG but with convergence at 48 layers instead of 64 layers.

Therefore, the study concludes that a minimum vertical resolution (roughly 48 isopycnal layers in this case) is required to minimize the impact on internal tide energetics and internal tide-induced vertical transport and shear, both important to the mixing of water masses and the subsequent consequences to sound speed variability and underwater acoustic propagation for the configurations of these simulations (1-km horizontal grid-spacing).

Realistic ocean models are often used to make acoustic predictions in a similar way as done here. However, the influence of ocean simulation choices—especially horizontal and vertical grid resolution—on these predictions is often overlooked. As ocean models improve, secondary users like acousticians need to assess how model choices, such as vertical grid discretizations, affect their acoustic prediction. Our results show that the greater number of layers leads to different convergence zones and transmission in acoustic ducts. Here, we show only transmission loss; however, acoustic arrival time, the time it takes a signal to propagate underwater, is another metric that can be essential for a number of applications (e.g., detection/ranging), and would equally be affected. Similarly, acoustic predictions that are limited by Central Processing Units (such as autonomous vehicles) may use results like these to understand how acoustic predictions in ocean simulations featuring less vertical layers would differ from predictions in simulations featuring more vertical layers.

Our findings are particularly relevant to the tropical region, as the density profile used in our simulations represents a typical density field of tropical oceans. Fewer layers may be required to resolve density profiles with weaker vertical gradients, such as those found in mid-latitude and polar regions. However, in the context of Ocean Global Circulation Models, a challenge arises when choosing the optimal vertical grid for the whole globe once the depths of the zero-crossings of the  $u$ -eigenfunction of a given mode will likely be different depending on the density field.

Similarly, our results are based on simulations with steep (supercritical) topography. The majority of the ocean, at least for the lowest modes (see Fig. 10 of Geoffroy et al., 2024), lies within the subcritical regime. This suggests that the analysis of supercritical slopes presented here should offer a reliable upper bound for internal tide generation processes across the global ocean. Furthermore, less steep slopes tend to produce more predictable and linear internal waves, while steeper, supercritical topographies lead to more complex nonlinear responses. Therefore, by finding vertical grids that effectively resolve more complex configurations—such as steeper bathymetry and stronger vertical density gradients—one can expect that internal tides generated in less complex (in terms of gradients) configurations will also be resolved. Additionally, in the case of realistic seafloor topographies, with many slopes, we can expect the generation of a continuum of spatial scales and a more broadly distributed energy conversion across modes. It is also important to note that the accurate representation of some flow-topography interactions, such as processes occurring in the bottom Ekman layer (e.g., Capó et al., 2024), would likely require a higher number of interface depths near the seafloor. We acknowledge that the 2-D nature of

the simulations, chosen to reduce computational costs without a meridional component, has some limitations as it only considers the zonal component of the tides and is not affected by meridional changes in the Coriolis parameter.

## Data Availability Statement

The simulations are available at <https://data.hycom.org/pub/lhiron/SMTa0.12/>. Bellhop 3D, used to model acoustic propagation, is available from the Ocean Acoustics Laboratory Acoustic Toolbox (<http://oalib.hlsresearch.com/AcousticsToolbox>; Porter, 2011). The density profile used to initialize the simulations is from the World Ocean Atlas 2018 (<https://www.ncei.noaa.gov/products/world-ocean-atlas>).

## References

- Alford, M. H., & Zhao, Z. (2007). Global patterns of low-mode internal-wave propagation. Part I: Energy and energy flux. *Journal of Physical Oceanography*, 37(7), 1829–1848. <https://doi.org/10.1175/jpo3085.1>
- Arbic, B. K. (2022). Incorporating tides and internal gravity waves within global ocean general circulation models: A review. *Progress in Oceanography*, 206, 102824. <https://doi.org/10.1016/j.pocean.2022.102824>
- Arbic, B. K., Alford, M. H., Ansong, J. K., Buijsman, M. C., Ciotti, R. B., Farrar, J. T., et al. (2018). A primer on global internal tide and internal gravity wave continuum modeling in HYCOM and MITgcm. In E. Chassignet, A. Pascual, J. Tintore, & J. Verron (Eds.), *New frontiers in operational oceanography, GODAE OceanView* (pp. 307–392). <https://doi.org/10.17125/gov2018.ch13>
- Arbic, B. K., Richman, J. G., Shriver, J. F., Timko, P. G., Metzger, E. J., & Wallcraft, A. J. (2012). Global modeling of internal tides within an eddy ocean general circulation model. *Oceanography*, 25(2), 20–29. <https://doi.org/10.5670/oceanog.2012.38>
- Balmforth, N. J., Ierley, G. R., & Young, W. R. (2002). Tidal conversion by subcritical topography. *Journal of Physical Oceanography*, 32(10), 2900–2914. [https://doi.org/10.1175/1520-0485\(2002\)032<2900:tcbst>2.0.co;2](https://doi.org/10.1175/1520-0485(2002)032<2900:tcbst>2.0.co;2)
- Bleck, R. (2002). An oceanic general circulation model framed in hybrid isopycnic–Cartesian coordinates. *Ocean Modelling*, 37(1), 55–88. [https://doi.org/10.1016/s1463-5003\(01\)00012-9](https://doi.org/10.1016/s1463-5003(01)00012-9)
- Bourget, B., Dauxois, T., Joubaud, S., & Odier, P. (2013). Experimental study of parametric subharmonic instability for internal plane waves. *Journal of Fluid Mechanics*, 723, 1–20. <https://doi.org/10.1017/jfm.2013.78>
- Buijsman, M. C., Ansong, J. K., Arbic, B. K., Richman, J. G., Shriver, J. F., Timko, P. G., et al. (2016). Impact of parameterized internal wave drag on the semidiurnal energy balance in a global ocean circulation model. *Journal of Physical Oceanography*, 46(5), 1399–1419. <https://doi.org/10.1175/JPO-D-15-0074.1>
- Buijsman, M. C., Arbic, B. K., Richman, J. G., Shriver, J. F., Wallcraft, A. J., & Zamudio, L. (2017). Semidiurnal internal tide incoherence in the equatorial Pacific. *Journal of Geophysical Research: Oceans*, 122(7), 5286–5305. <https://doi.org/10.1002/2016JC012590>
- Buijsman, M. C., Kanarska, Y., & McWilliams, J. C. (2010). On the generation and evolution of nonlinear internal waves in the South China Sea. *Journal of Geophysical Research*, 115(C2), C02012. <https://doi.org/10.1029/2009JC005275>
- Buijsman, M. C., Klymak, J. M., Legg, S., Alford, M. H., Farmer, D., MacKinnon, J. A., et al. (2014). Three dimensional double ridge internal tide resonance in Luzon Strait. *Journal of Physical Oceanography*, 44(3), 850–869. <https://doi.org/10.1175/jpo-d-13-024.1>
- Buijsman, M. C., Stephenson, G. R., Ansong, J. K., Arbic, B. K., Green, M., Richman, J. G., et al. (2020). On the interplay between horizontal resolution and wave drag and their effect on tidal baroclinic mode waves in realistic global ocean simulations. *Ocean Modelling*, 152, 101656. <https://doi.org/10.1016/j.ocemod.2020.101656>
- Capó, E., McWilliams, J. C., Gula, J., Molemaker, M. J., Damien, P., & Schubert, R. (2024). Abyssal slope currents. *Journal of Physical Oceanography*, 54(11), 2373–2392. <https://doi.org/10.1175/JPO-D-24-0028.1>
- Chassignet, E. P., Hurlburt, H. E., Metzger, E. J., Smedstad, O. M., Cummings, J. A., Halliwell, G. R., et al. (2009). US GODAE: Global ocean prediction with the HYbrid Coordinate Ocean Model (HYCOM). *Oceanography*, 22(2), 64–75. <https://doi.org/10.5670/oceanog.2009.39>
- Chassignet, E. P., Smith, L. T., Halliwell, G. R., & Bleck, R. (2003). North Atlantic simulations with the Hybrid Coordinate Ocean Model (HYCOM): Impact of the vertical coordinate choice, reference pressure, and thermobaricity. *Journal of Physical Oceanography*, 33(12), 2504–2526. [https://doi.org/10.1175/1520-0485\(2003\)033<2504:NASWTH>2.0.CO;2](https://doi.org/10.1175/1520-0485(2003)033<2504:NASWTH>2.0.CO;2)
- Chassignet, E. P., & Xu, X. (2017). Impact of horizontal resolution (1/12° to 1/50°) on Gulf Stream separation, penetration, and variability. *Journal of Physical Oceanography*, 47(8), 1999–2021. <https://doi.org/10.1175/JPO-D-17-0031.1>
- Chassignet, E. P., Xu, X., Bozec, A., & Uchida, T. (2023). Impact of the New England seamount chain on Gulf Stream pathway and variability. *Journal of Physical Oceanography*, 53(8), 1871–1886. <https://doi.org/10.1175/JPO-D-23-0008.1>
- Colosi, J. A., Chandrayadula, T., Coby, W., Fischer, J., Dushaw, B. D., Dzieciuch, M. A., & Worcester, P. F. (2013). The effects of internal tides on phase and amplitude statistics in the Philippine Sea. *Journal of the Acoustical Society of America*, 133(5\_Supplement), 3345. <https://doi.org/10.1121/1.4805663>
- Colosi, J. A., & Rudnick, D. L. (2020). Observations of upper ocean sound-speed structures in the North Pacific and their effects on long-range acoustic propagation at low and mid-frequencies. *Journal of the Acoustical Society of America*, 148(4), 2040–2060. <https://doi.org/10.1121/1.0002174>
- Dauxois, T., Joubaud, S., Odier, P., & Venaille, A. (2018). Instabilities of internal gravity wave beams. *Annual Review of Fluid Mechanics*, 50(1), 131–156. <https://doi.org/10.1146/annurev-fluid-122316-044539>
- de Lavergne, C., Vic, C., Madec, G., Roquet, F., Waterhouse, A. F., Whalen, C. B., et al. (2020). A parameterization of local and remote tidal mixing. *Journal of Advances in Modeling Earth Systems*, 12(5), e2020MS002065. <https://doi.org/10.1029/2020MS002065>
- Dushaw, B. D., Howe, B. M., Cornuelle, B. D., Worcester, P. F., & Luther, D. S. (1995). Barotropic and baroclinic tides in the central North Pacific Ocean determined from long-range reciprocal acoustic transmissions. *Journal of Physical Oceanography*, 25(4), 631–647. [https://doi.org/10.1175/1520-0485\(1995\)025<0631:babtit>2.0.co;2](https://doi.org/10.1175/1520-0485(1995)025<0631:babtit>2.0.co;2)
- Early, J. J., Lelong, M. P., & Smith, K. S. (2020). Fast and accurate computation of vertical modes. *Journal of Advances in Modeling Earth Systems*, 12(2), e2019MS001939. <https://doi.org/10.1029/2019MS001939>
- Early, J. J., Lelong, M. P., & Sundermeyer, M. A. (2021). A generalized wave-vortex decomposition for rotating Boussinesq flows with arbitrary stratification. *Journal of Fluid Mechanics*, 912, A32. <https://doi.org/10.1017/jfm.2020.995>

## Acknowledgments

LH would like to thank Edward Zaron for his helpful comments and Dheeraj Varma for the discussions on PSI. We would like to thank three anonymous reviewers for their valuable comments and suggestions. We acknowledge financial support from an Office of Naval Research (ONR) Task Force Ocean (TFO) project that the authors participated in. The ONR Grants for this TFO project are N00014-19-1-2717 (LH, KJR, EPC, AB), N00014-20-C-2018 (MCS, EFC), N00014-19-1-2704 (MCB, MSS), and N00014-19-1-2712 (BKA).

- Eden, C., Pollmann, F., & Olbers, D. (2020). Towards a global spectral energy budget for internal gravity waves in the ocean. *Journal of Physical Oceanography*, 50(4), 935–944. <https://doi.org/10.1175/JPO-D-19-0022.1>
- Egbert, G. D., & Ray, R. D. (2003). Semi-diurnal and diurnal tidal dissipation from TOPEX/Poseidon altimetry. *Geophysical Research Letters*, 30(17), 1907. <https://doi.org/10.1029/2003GL017676>
- Erbe, C., Duncan, A., & Vigness-Raposa, K. J. (2022). Introduction to sound propagation under water. In C. Erbe & J. A. Thomas (Eds.), *Exploring animal behavior through sound* (Vol. 1, pp. 185–216). Springer. [https://doi.org/10.1007/978-3-030-97540-1\\_6](https://doi.org/10.1007/978-3-030-97540-1_6)
- Ferrari, R., & Wunsch, C. (2009). Ocean circulation kinetic energy: Reservoirs, sources, and sinks. *Annual Review of Fluid Mechanics*, 41(1), 253–282. <https://doi.org/10.1146/annurev.fluid.40.111406.102139>
- Garcia, H. E., Boyer, T. P., Baranova, O. K., Locarnini, R. A., Mishonov, A. V., Grodsky, A., et al. (2019). In A. Mishonov (Ed.), *World Ocean Atlas 2018: Product Documentation*. Retrieved from <https://data.nodc.noaa.gov/woa/WOA18/DOC/woa18documentation.pdf>
- Garrett, C., & Kunze, E. (2007). Internal tide generation in the deep ocean. *Annual Review of Fluid Mechanics*, 39(1), 57–87. <https://doi.org/10.1146/annurev.fluid.39.050905.110227>
- Geoffroy, G., Pollmann, F., & Nycander, J. (2024). Tidal conversion into vertical normal modes by near-critical topography. *Journal of Physical Oceanography*, 54(9), 1949–1970. <https://doi.org/10.1175/JPO-D-23-0255.1>
- Gerkema, T., & Zimmerman, J. T. F. (2008). *An introduction to internal waves, Lecture Notes* (p. 207). Royal NIOZ.
- Gill, A. E. (1982). *Atmosphere-ocean dynamics* (Vol. 30). Academic Press.
- Griffies, S. M., & Treguier, A. M. (2013). Ocean circulation models and modeling. *International Geophysics*, 103, 521–551. <https://doi.org/10.1016/b978-0-12-391851-2.00020-9>
- Hebert, D. (1994). Closing a heat budget: Effect of internal waves. *Deep Sea Research Part I: Oceanographic Research Papers*, 41(1), 1–8. [https://doi.org/10.1016/0967-0637\(94\)90023-X](https://doi.org/10.1016/0967-0637(94)90023-X)
- Helber, R. W., Kara, A. B., Richman, J. G., Carnes, M. R., Barron, C. N., Hurlburt, H. E., & Boyer, T. (2012). Temperature versus salinity gradients below the ocean mixed layer. *Journal of Geophysical Research*, 117(C5), C05006. <https://doi.org/10.1029/2011JC007382>
- Hiron, L., Miron, P., Shay, L. K., Johns, W. E., Chassignet, E. P., & Bozec, A. (2022). Lagrangian coherence and source of water of Loop Current Frontal Eddies in the Gulf of Mexico. *Progress in Oceanography*, 208, 102876. <https://doi.org/10.1016/j.poccean.2022.102876>
- Hiron, L., Nolan, D. S., & Shay, L. K. (2021). Study of ageostrophy during strong, nonlinear eddy-front interaction in the Gulf of Mexico. *Journal of Physical Oceanography*, 51(3), 745–755. <https://doi.org/10.1175/JPO-D-20-0182.1>
- Jalali, M., Rapaka, N. R., & Sarkar, S. (2014). Tidal flow over topography: Effect of excursion number on wave energetics and turbulence. *Journal of Fluid Mechanics*, 750, 259–283. <https://doi.org/10.1017/jfm.2014.258>
- Joubaud, S., Munroe, J., Odier, P., & Dauxois, T. (2012). Experimental parametric subharmonic instability in stratified fluids. *Physics of Fluids*, 24(4), 041703. <https://doi.org/10.1063/1.4706183>
- Kang, D., & Fringer, O. (2010). On the calculation of available potential energy in internal wave fields. *Journal of Physical Oceanography*, 40(11), 2539–2545. <https://doi.org/10.1175/2010JPO4497.1>
- Kelly, S. M. (2016). The vertical mode decomposition of surface and internal tides in the presence of a free surface and arbitrary topography. *Journal of Physical Oceanography*, 46(12), 3777–3788. <https://doi.org/10.1175/JPO-D-16-0131.1>
- Kelly, S. M., & Lermusiaux, P. F. (2016). Internal-tide interactions with the Gulf Stream and middle Atlantic bight shelfbreak front. *Journal of Geophysical Research: Oceans*, 121(8), 6271–6294. <https://doi.org/10.1002/2016JC011639>
- Kelly, S. M., Nash, J. D., Martini, K. I., Alford, M. H., & Kunze, E. (2012). The cascade of tidal energy from low to high modes on a continental slope. *Journal of Physical Oceanography*, 42(7), 1217–1232. <https://doi.org/10.1175/JPO-D-11-0231.1>
- Klymak, J. M., Alford, M. H., Pinkel, R., Lien, R., Yang, Y. J., & Tang, T. (2011). The breaking and scattering of the internal tide on a continental slope. *Journal of Physical Oceanography*, 41(5), 926–945. <https://doi.org/10.1175/2010JPO4500.1>
- Kossack, J., Mathis, M., Daewel, U., Zhang, Y. J., & Schrum, C. (2023). Barotropic and baroclinic tides increase primary production on the Northwest European Shelf. *Frontiers in Marine Science*, 10, 2296–7745. <https://doi.org/10.3389/fmars.2023.1206062>
- Koudella, C., & Staquet, C. (2006). Instability mechanisms of a two-dimensional progressive internal gravity wave. *Journal of Fluid Mechanics*, 548(1), 165–196. <https://doi.org/10.1017/S0022112005007524>
- Kundu, P. K. (1990). *Fluid mechanics* (p. 638). Academic Press.
- Lamb, K. G. (2004). Nonlinear interaction among internal wave beams generated by tidal flow over supercritical topography. *Geophysical Research Letters*, 31(9), L09313. <https://doi.org/10.1029/2003GL019393>
- Large, W. G., McWilliams, J. C., & Doney, S. C. (1994). Oceanic vertical mixing: A review and a model with a nonlocal boundary layer parameterization. *Reviews of Geophysics*, 32(4), 363–403. <https://doi.org/10.1029/94RG01872>
- Le Sommer, J., Chassignet, E. P., & Wallcraft, A. J. (2018). Ocean circulation modeling for operational oceanography: Current status and future challenges. In E. Chassignet, A. Pascual, J. Tintoré, & J. Verron (Eds.), *New Frontiers in Operational Oceanography, GODAE OceanView* (pp. 289–306). <https://doi.org/10.17125/gov2018.ch12>
- Mackenzie, K. V. (1981). Nine-term equation for sound speed in the oceans. *Journal of the Acoustical Society of America*, 70(3), 807–812. <https://doi.org/10.1121/1.386920>
- MacKinnon, J. A., & Gregg, M. C. (2003). Shear and baroclinic energy flux on the summer New England shelf. *Journal of Physical Oceanography*, 33(7), 1462–1475. [https://doi.org/10.1175/1520-0485\(2003\)033<1462:SABEFO>2.0.CO;2](https://doi.org/10.1175/1520-0485(2003)033<1462:SABEFO>2.0.CO;2)
- MacKinnon, J. A., Zhao, Z., Whalen, C. B., Waterhouse, A. F., Trossman, D. S., Sun, O. M., et al. (2017). Climate process team on internal wave-driven ocean mixing. *Bulletin of the American Meteorological Society*, 98(11), 2429–2454. <https://doi.org/10.1175/BAMS-D-16-0030.1>
- Madec, G., Bourdallé-Badie, R., Chanut, J., Clementi, E., Coward, A., Ethé, C., et al. (2019). NEMO ocean engine. In *Notes du Pôle de modélisation de l'Institut Pierre-Simon Laplace (IPSL) (v4.0)* (Vol. 27). Zenodo. <https://doi.org/10.5281/zenodo.3878122>
- Melet, A., Hallberg, R., & Marshall, D. P. (2022). Chapter 2 – The role of ocean mixing in the climate system. In M. Meredith & A. Naveira Garabato (Eds.), *Ocean mixing* (pp. 5–34). Elsevier. <https://doi.org/10.1016/B978-0-12-821512-8.00009-8>
- Munk, W., & Wunsch, C. (1998). Abyssal recipes II: Energetics of tidal and wind mixing. *Deep-Sea Research I*, 45(12), 1977–2010. [https://doi.org/10.1016/s0967-0637\(98\)00070-3](https://doi.org/10.1016/s0967-0637(98)00070-3)
- Nelson, A., Arbic, B., Menemenlis, D., Peltier, W., Alford, M., Grisouard, N., & Klymak, J. (2020). Improved internal wave spectral continuum in a regional ocean model. *Journal of Geophysical Research: Oceans*, 125(5), e2019JC015974. <https://doi.org/10.1029/2019JC015974>
- Nelson, A. D., Arbic, B. K., Zaron, E. D., Savage, A. C., Richman, J. G., Buijsman, M. C., & Shriver, J. F. (2019). Toward realistic nonstationarity of semidiurnal baroclinic tides in a hydrodynamic model. *Journal of Geophysical Research: Oceans*, 124(9), 6632–6642. <https://doi.org/10.1029/2018JC014737>
- Noufal, K. K., Sanjana, M. C., Latha, G., & Ramesh, R. (2022). Influence of internal wave induced sound speed variability on acoustic propagation in shallow waters of North West Bay of Bengal. *Applied Acoustics*, 194, 108778. <https://doi.org/10.1016/j.apacoust.2022.108778>



- Olbbers, D., Eden, C., Becker, E., Pollmann, F., & Jungclauss, J. (2019). The IDEMIX model: Parameterization of internal gravity waves for circulation models of ocean and atmosphere. In C. Eden & A. Iske (Eds.), *Energy Transfers in Atmosphere and Ocean. Mathematics of Planet Earth* (Vol. 1, pp. 87–125). Springer. [https://doi.org/10.1007/978-3-030-05704-6\\_3](https://doi.org/10.1007/978-3-030-05704-6_3)
- Park, Y.-H., Fuda, J.-L., Durand, I., & Garabato, A. C. N. (2008). Internal tides and vertical mixing over the Kerguelen Plateau. *Deep Sea Research Part II: Topical Studies in Oceanography*, 55(5–7), 582–593. <https://doi.org/10.1016/j.dsr2.2007.12.027>
- Ponte, A. L., & Klein, P. (2015). Incoherent signature of internal tides on sea level in idealized numerical simulations. *Geophysical Research Letters*, 42(5), 1520–1526. <https://doi.org/10.1002/2014GL025833>
- Porter, M. (2011). The BELLHOP manual and user's guide: Preliminary draft. Retrieved from <http://oalib.hlsresearch.com/Rays/HLS-2010-1.pdf>
- Preisig, J. (2007). Acoustic propagation considerations for underwater acoustic communications network development. *ACM SIGMOBILE Mobile Computing and Communications Review*, 11(4), 2–10. <https://doi.org/10.1145/1347364.1347370>
- Rainville, L., Johnston, T. M. S., Carter, G. S., Merrifield, M. A., Pinkel, R., Worcester, P. F., & Dushaw, B. D. (2010). Interference pattern and propagation of the  $M_2$  internal tide south of the Hawaiian Ridge. *Journal of Physical Oceanography*, 40(2), 311–325. <https://doi.org/10.1175/2009JPO4256.1>
- Rainville, L., Lee, C. M., Rudnick, D. L., & Yang, K.-C. (2013). Propagation of internal tides generated near Luzon Strait: Observations from autonomous gliders. *Journal of Geophysical Research: Oceans*, 118(9), 4125–4138. <https://doi.org/10.1002/jgrc.20293>
- Rainville, L., & Pinkel, R. (2006). Propagation of low-mode internal waves through the ocean. *Journal of Physical Oceanography*, 36(6), 1220–1236. <https://doi.org/10.1175/jpo2889.1>
- Raja, K. J., Buijsman, M. C., Bozec, A., Helber, R. W., Shriver, J. F., Wallcraft, A., et al. (2024). Spurious internal wave generation during data assimilation in eddy resolving ocean model simulations. *Ocean Modelling*, 188, 102340. <https://doi.org/10.1016/j.ocemod.2024.102340>
- Raja, K. J., Buijsman, M. C., Shriver, J. F., Arbic, B. K., & Siyanbola, O. (2022). Near-inertial wave energetics modulated by background flows in a global model simulation. *Journal of Physical Oceanography*, 52(5), 823–840. <https://doi.org/10.1175/jpo-d-21-0130.1>
- Ray, R. D., & Mitchum, G. T. (1996). Surface manifestation of internal tides generated near Hawaii. *Geophysical Research Letters*, 23(16), 2101–2104. <https://doi.org/10.1029/96gl02050>
- Ray, R. D., & Mitchum, G. T. (1997). Surface manifestation of internal tides in the deep ocean: Observations from altimetry and island gauges. *Progress in Oceanography*, 40(1), 135–162. [https://doi.org/10.1016/s0079-6611\(97\)00025-6](https://doi.org/10.1016/s0079-6611(97)00025-6)
- Ray, R. D., & Zaron, E. D. (2011). Non-stationary internal tides observed with satellite altimetry. *Geophysical Research Letters*, 38(17), L17609. <https://doi.org/10.1029/2011GL048617>
- Shriver, J. F., Richman, J. G., & Arbic, B. K. (2014). How stationary are the internal tides in a high-resolution global ocean circulation model? *Journal of Geophysical Research: Oceans*, 119(5), 2769–2787. <https://doi.org/10.1002/2013JC009423>
- Skamarock, W. C. (2004). Evaluating mesoscale NWP models using kinetic energy spectra. *Monthly Weather Review*, 132(12), 3019–3032. <https://doi.org/10.1175/MWR2830.1>
- Solano, M. S., Buijsman, M. C., Shriver, J. F., Magalhaes, J., da Silva, J., Jackson, C., et al. (2023). Nonlinear internal tides in a realistically forced global ocean simulation. *Journal of Geophysical Research: Oceans*, 128(12), e2023JC019913. <https://doi.org/10.1029/2023JC019913>
- Soufflet, Y., Marchesiello, P., Lemarié, F., Jouanno, J., Capet, X., Debreu, L., & Benshila, R. (2016). On effective resolution in ocean models. *Ocean Modelling*, 98, 36–50. <https://doi.org/10.1016/j.ocemod.2015.12.004>
- Staquet, C., & Sommeria, J. (2002). Internal gravity waves: From instabilities to turbulence. *Annual Review of Fluid Mechanics*, 34(1), 559–593. <https://doi.org/10.1146/annurev.fluid.34.090601.130953>
- Stewart, K. D., Hogg, A. M., Griffies, S. M., Heerdegen, A. P., Ward, M. L., Spence, P., & England, M. H. (2017). Vertical resolution of baroclinic modes in global ocean models. *Ocean Modelling*, 113, 50–65. <https://doi.org/10.1016/j.ocemod.2017.03.012>
- Stewart, K. D., Hughes, G. O., & Griffiths, R. W. (2012). The role of turbulent mixing in an overturning circulation maintained by surface buoyancy forcing. *Journal of Physical Oceanography*, 42(11), 1907–1922. <https://doi.org/10.1175/JPO-D-11-0242.1>
- St. Laurent, L., & Garrett, C. (2002). The role of internal tides in mixing the deep ocean. *Journal of Physical Oceanography*, 32(10), 2882–2899. [https://doi.org/10.1175/1520-0485\(2002\)032<2882:TROI>2.0.CO;2](https://doi.org/10.1175/1520-0485(2002)032<2882:TROI>2.0.CO;2)
- Sutherland, B. R., & Dhaliwal, M. S. (2022). The nonlinear evolution of internal tides. Part 1: The superharmonic cascade. *Journal of Fluid Mechanics*, 948, A21. <https://doi.org/10.1017/jfm.2022.689>
- Sutherland, B. R., & Jefferson, R. (2020). Triad resonant instability of horizontally periodic internal modes. *Physical Review Fluids*, 5(3), 034801. <https://doi.org/10.1103/PhysRevFluids.5.034801>
- Thakur, R., Arbic, B. K., Menemenlis, D., Momeni, K., Pan, Y., Peltier, W. R., et al. (2022). Impact of vertical mixing parameterizations on internal gravity wave spectra in regional ocean models. *Geophysical Research Letters*, 49(16), e2022GL099614. <https://doi.org/10.1029/2022GL099614>
- Tuerena, R. E., Williams, R. G., Mahaffey, C., Vic, C., Green, J. A. M., Naveira-Garabato, A., et al. (2019). Internal tides drive nutrient fluxes into the deep chlorophyll maximum over mid-ocean ridges. *Global Biogeochemical Cycles*, 33(8), 995–1009. <https://doi.org/10.1029/2019GB006214>
- Turgut, A., Mignerey, P. C., Goldstein, D. J., & Schindall, J. A. (2013). Acoustic observations of internal tides and tidal currents in shallow water. *Journal of the Acoustical Society of America*, 133(4), 1981–1986. <https://doi.org/10.1121/1.4792141>
- Uchida, T., Le Sommer, J., Stern, C., Abernathey, R. P., Holdgraf, C., Albert, A., et al. (2022). Cloud-based framework for inter-comparing submesoscale-permitting realistic ocean models. *Geoscientific Model Development*, 15(14), 5829–5856. <https://doi.org/10.5194/gmd-15-5829-2022>
- Urlick, R. J. (1982). *Sound propagation in the sea*. Peninsula Publishing.
- Varma, D., & Mathur, M. (2017). Internal wave resonant triads in finite-depth non-uniform stratifications. *Journal of Fluid Mechanics*, 824, 286–311. <https://doi.org/10.1017/jfm.2017.343>
- Varma, D., Mathur, M., & Dauxois, T. (2023). Instabilities in internal gravity waves. *Mathematics in Engineering*, 5(1), 1–34. <https://doi.org/10.3934/mine.2023016>
- Vic, C., Naveira Garabato, A. C., Green, J. A. M., Waterhouse, A. F., Zhao, Z., Melet, A., et al. (2019). Deep-ocean mixing driven by small-scale internal tides. *Nature Communications*, 10(1), 2099. <https://doi.org/10.1038/s41467-019-10149-5>
- Wang, Y., & Legg, S. (2023). Enhanced dissipation of internal tides in a mesoscale baroclinic eddy. *Journal of Physical Oceanography*, 53(10), 2293–2316. <https://doi.org/10.1175/JPO-D-23-0045.1>
- Wunsch, C. (1975). Internal tides in the ocean. *Reviews of Geophysics*, 13(1), 167–182. <https://doi.org/10.1029/RG013i001p00167>
- Xu, X., Chassignet, E. P., & Wallcraft, A. J. (2023). Impact of vertical resolution on representing baroclinic modes and water mass distribution in the North Atlantic circulation. *Ocean Modelling*, 186, 102261. <https://doi.org/10.1016/j.ocemod.2023.102261>

- Xu, X., Chassignet, E. P., Wallcraft, A. J., Arbic, B. K., Buijsman, M. C., & Solano, M. (2022). On the spatial variability of the mesoscale sea surface height wavenumber spectra in the Atlantic Ocean. *Journal of Geophysical Research: Oceans*, *127*(10), e2022JC018769. <https://doi.org/10.1029/2022JC018769>
- Yadidya, B., Arbic, B. K., Shriver, J. F., Nelson, A. D., Zaron, E. D., Buijsman, M. C., & Thakur, R. (2024). Phase-accurate internal tides in a global ocean forecast model: Potential applications for nadir and wide-swath altimetry. *Geophysical Research Letters*, *51*(4), e2023GL107232. <https://doi.org/10.1029/2023GL107232>
- Yang, J., Rouseff, D., Tang, D., & Henyey, F. S. (2010). Effect of the internal tide on acoustic transmission loss at midfrequencies. *IEEE Journal of Oceanic Engineering*, *35*(1), 3–11. <https://doi.org/10.1109/JOE.2009.2038984>
- Zaron, E. D. (2017). Mapping the nonstationary internal tide with satellite altimetry. *Journal of Geophysical Research: Oceans*, *122*(1), 539–554. <https://doi.org/10.1002/2016JC012487>
- Zaron, E. D., & Egbert, G. D. (2014). Time-variable refraction of the internal tide at the Hawaiian Ridge. *Journal of Physical Oceanography*, *44*(2), 538–557. <https://doi.org/10.1175/JPO-D-12-0238.1>